nature physics

Article

https://doi.org/10.1038/s41567-024-02632-8

Dynamic traction force measurements of migrating immune cells in 3D biopolymer matrices

Received: 8 September 2023

Accepted: 6 August 2024

Published online: 24 September 2024

Check for updates

David Böhringer[1], Mar Cóndor[2,3], Lars Bischof[1], Tina Czerwinski[1], Niklas Gampl[4,5], Phuong Anh Ngo[6,7], Andreas Bauer[1], Caroline Voskens[7,8], Rocío López-Posadas[6,7], Kristian Franze[4,5,9], Silvia Budday[10], Christoph Mark[1], Ben Fabry[1] ✉ & Richard Gerum[1,11]

Immune cells, such as natural killer cells, migrate with high speeds of several micrometres per minute through dense tissue. However, the magnitude of the traction forces during this migration is unknown. Here we present a method to measure dynamic traction forces of fast migrating cells in biopolymer matrices from the observed matrix deformations. Our method accounts for the mechanical nonlinearity of the three-dimensional tissue matrix and can be applied to time series of confocal or bright-field image stacks. It allows for precise force reconstruction over a wide range of force magnitudes and object sizes—even when the imaged volume captures only a small part of the matrix deformation field. We demonstrate the broad applicability of our method by measuring forces from around 1 nN for axon growth cones up to around 10 μN for mouse intestinal organoids. We find that natural killer cells show bursts of large traction forces around 50 nN that increase with matrix stiffness. These force bursts are driven by myosin II contractility, mediated by integrin β1 adhesions, focal adhesion kinase and Rho-kinase activity, and occur predominantly when the cells migrate through narrow matrix pores.

Essential cell functions such as migration and spreading require that cells exert traction forces on their extracellular matrix. Several traction force microscopy (TFM) methods exist that measure the force-induced deformations of the extracellular matrix and reconstruct the cell forces based on continuum mechanical principles. Mathematically, the computation of forces from matrix deformations is an inverse problem where small measurement noise can give rise to large erroneous forces. This is typically solved by various smoothing or force regularization methods[1–3]. For cells grown on two-dimensional (flat) matrices with linear elastic properties, such as polyacrylamide hydrogels or silicone elastomers, robust and computationally inexpensive methods have been developed[4–7]. The force reconstruction problem becomes considerably more difficult in three dimensions[2,8–11], especially in the case of mechanically nonlinear materials, such as collagen or fibrin hydrogels[12–18], which are frequently used as a three-dimensional (3D) matrix for cell culture.

Current 3D force reconstruction methods typically require the recording of a large 3D image stack around a cell that is sufficiently far away from other cells. In addition, knowledge of the cell surface (Fig. 1a, top), where by definition the traction forces are located, is also required for most methods. Staining and 3D imaging the cell surface, however, can affect cell behaviour or cause photodamage. All current methods require knowledge of the force-free reference configuration of the matrix, which is obtained either by detaching the cell from the matrix, by the addition of drugs that suppress cell forces (for example, cytochalasin D) or by killing the cell, for example, with high-intensity

A full list of affiliations appears at the end of the paper. ✉e-mail: ben.fabry@fau.de

https://doi.org/10.1038/s41567-024-02632-8

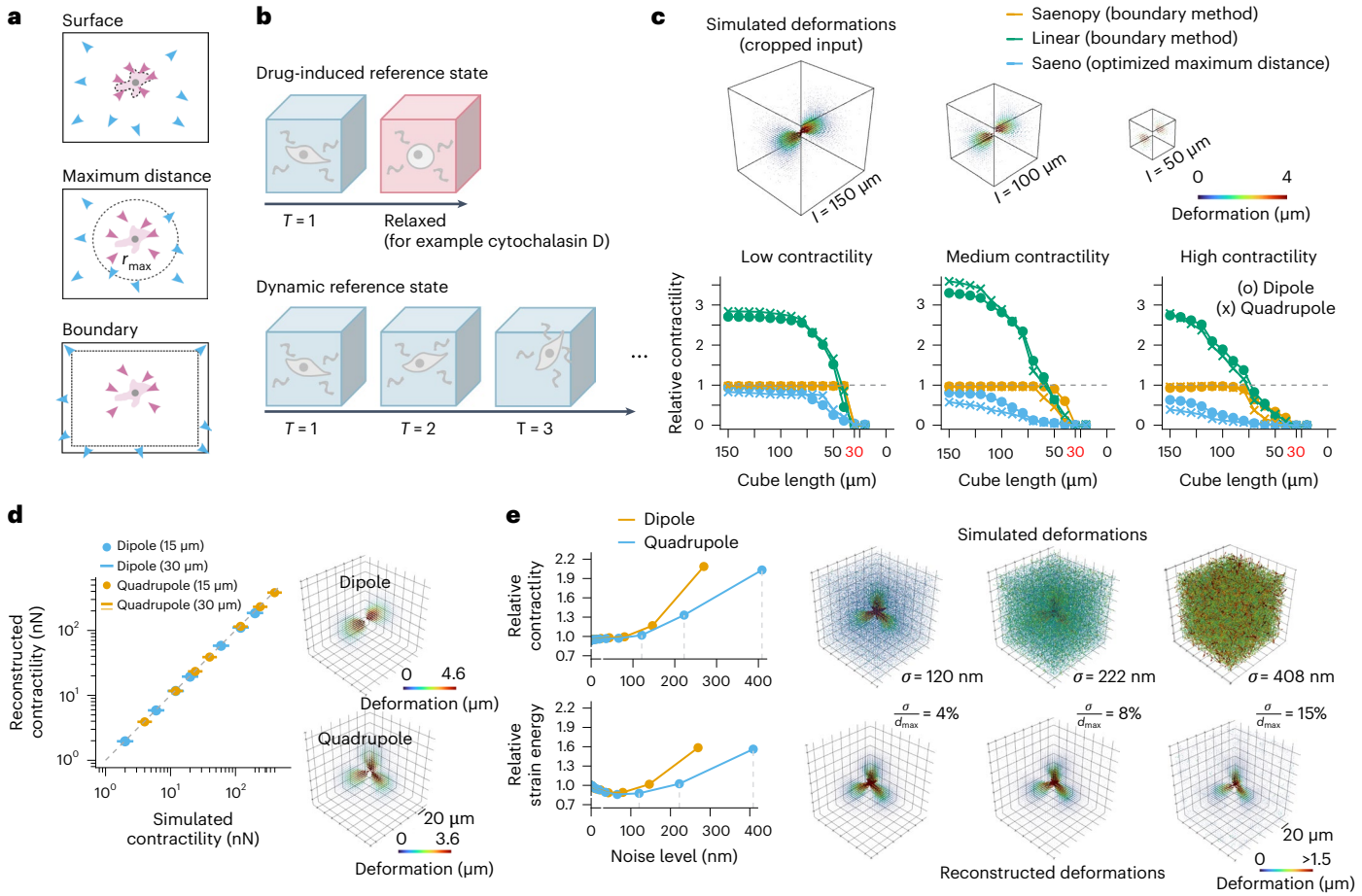

Fig. 1 | Material model for a nonlinear fibre matrix. a, Schematic of different regularization strategies. Top: traction forces (purple) are constrained to the cell surface. Middle: body forces are reconstructed by global regularization without knowledge of the cell surface. Forces within a distance (r_{max}, dotted grey line) around the force epicentre are considered cell-generated forces (purple); forces beyond r_{max} are considered balancing forces (blue) that account for noise, drift or nearby contractile cells. Bottom: Saenopy reconstructs body forces by global regularization except for the boundary regions, ensuring that balancing forces appear only at the boundaries. **b**, Methods for measuring the force-free matrix configuration. Top: cell forces are relaxed, for example, by actin-depolymerizing drugs. Three-dimensional matrix deformations are obtained at a single time point $T = 1$ from two image stacks recorded before and after drug treatment. Bottom: the force-free matrix configuration is computed from the cumulative matrix displacements between consecutive image stacks of a time series $T = 1, 2, 3...$, median-averaged over the observation period. Dynamic matrix deformations are obtained from the cumulative matrix displacements relative to the median average. **c**, Influence of image volume on force reconstruction accuracy. Cells are simulated using dipole (circles) or quadrupole (crosses) forces of low (3 nN), medium (30 nN) and high (100 nN) magnitude, with a distance of 30 µm between force monopoles (red *x*-axis label). The imaged volume is reduced from $(150\ \mu m)^3$ to $(20\ \mu m)^3$. The accuracy of force reconstruction is compared between Saenopy (boundary method, orange), Saenopy assuming linear elastic material behaviour (boundary method, green) and Saeno (maximum distance method with optimized r_{max}, blue). The dashed lines indicate the ground truth. The top images show exemplary deformation fields (coloured arrows) for a dipole with medium contractility at different cube lengths (l). **d**, Accuracy of force reconstruction for simulated dipoles (top inset) and quadrupoles (bottom inset) for different contractilities (sum of the force monopoles, spaced either 15 µm or 30 µm apart). The dashed grey line shows the line of identity. **e**, Influence of noise on force reconstruction (top left) and strain energy (bottom left), relative to ground-truth values, for simulated dipoles (20 nN contractility) or quadrupoles (40 nN contractility). Maximum matrix deformations (d_{max}) are around 3 µm in both cases. Gaussian noise with specified standard deviation σ is added to the deformation field (top right images for three selected noise values indicated by grey dashed lines). The bottom right images show reconstructed deformation fields.

laser light (Fig. 1b, top). Such methods therefore pose limitations for measuring multiple cells in a culture dish or for rapidly moving cells, such as immune cells.

Immune cells are known to migrate in a so-called amoeboid mode with limited or no proteolytic activity and with limited or no specific (for example, integrin mediated) adhesion to the extracellular matrix[19–21]. Therefore, it is assumed that immune cells do not generate appreciable traction forces during migration. Recent studies have indicated the involvement of integrin-mediated adhesions during immune cell migration[22–24], but due to the considerable technical challenges and limitations of existing methods, the traction forces of fast-moving immune cells through 3D tissues are not known[25].

Dynamic 3D TFM

Here we overcome these limitations by a locally adjusted regularization approach and by obtaining the force-free reference configuration of the matrix from time-lapse images. Our method builds on a previously developed nonlinear semi-affine network optimizer (Saeno)[12]. This method considers the nonlinear elastic behaviour of fibre matrices (Extended Data Fig. 1) and iteratively minimizes the discrepancy between measured and reconstructed matrix deformations (Fig. 1a, middle) by adjusting point forces that can appear anywhere in the volume but are regularized to favour few, large forces that are typically located near the cell body. Cell forces are then summed over a user-defined sphere around the cell[12,26]. One advantage of this approach is that the exact position of the cell surface does not need to be known.

https://doi.org/10.1038/s41567-024-02632-8

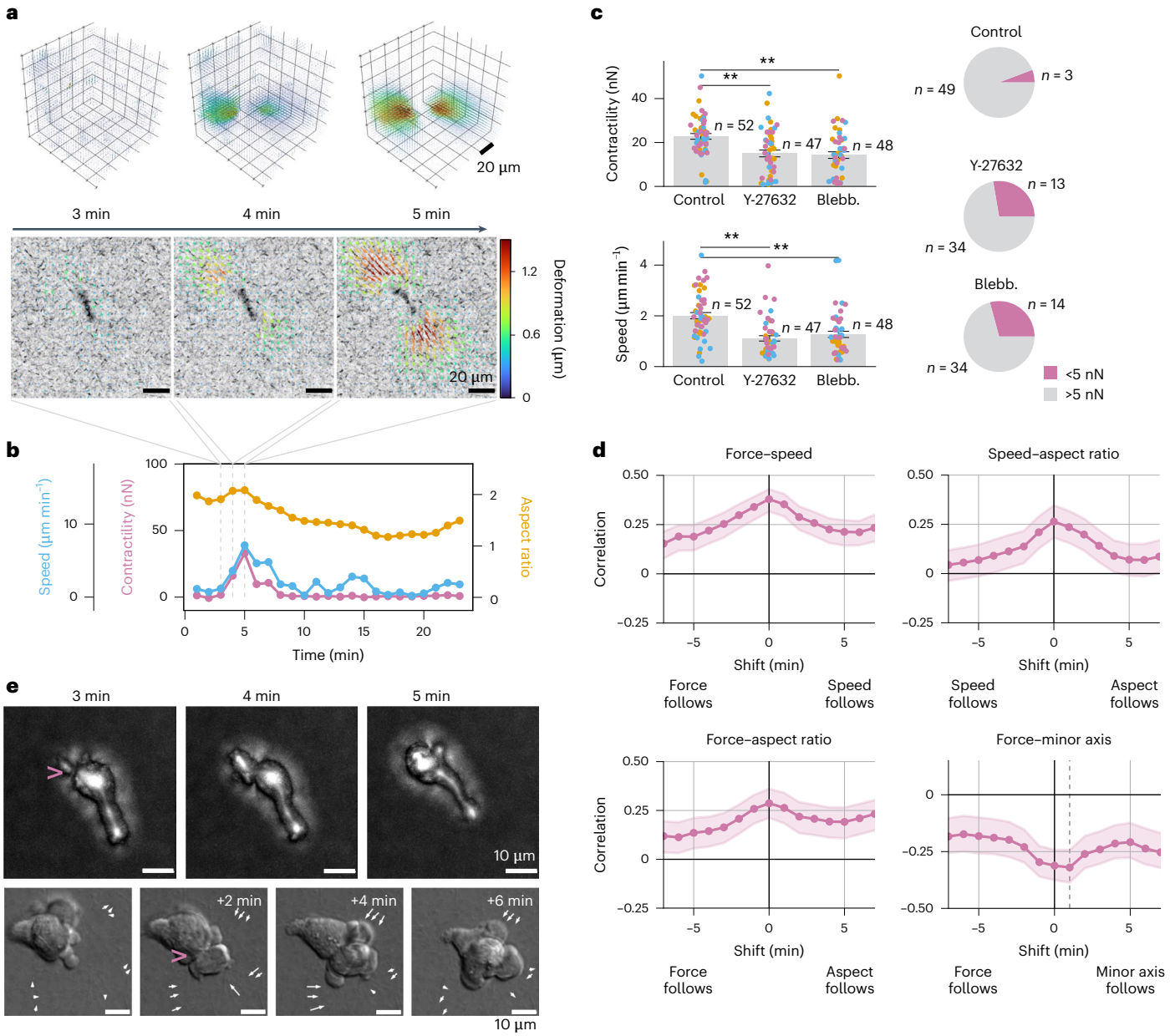

Fig. 2 | Contractile phases during NK cell migration. a, Top: matrix deformations around an NK cell migrating in 1.2 mg ml^{-1} collagen at different time points. Bottom: corresponding maximum-intensity projected confocal reflection images (inverted greyscale) overlaid with the matrix deformation field (indicated by coloured arrows). **b**, Cell speed (blue), cell aspect ratio (1, round; >1, elongated; orange) and cell contractility (pink) over a 23 min period. The dashed grey lines indicate the time points shown in **a**. **c**, Compared with the control, cells treated with Rho-kinase inhibitor Y-27632 (10 µM) or myosin II inhibitor blebbistatin (Blebb., 3 µM) show a decrease in maximum contractility (top left, mean ± s.e.), decrease in speed (bottom left, mean ± s.e.) and a decrease in the fraction of contractile cells (right) with a contractility >5 nN. Measurements of individual cells are shown as points and colours indicate independent experiments from different days. $^{**}P < 0.01$ for two-sided *t*-test with Bonferroni correction[51]. **d**, Cross-correlation between time courses of speed and force (top left), speed and aspect ratio (top right), force and aspect ratio (bottom left), and force and the minor cell axis (normalized to the square root of the cell area; bottom right). Signals are shifted relative to each other by ±5 min. The physical meaning of a positive correlation for different time shifts is indicated below the diagrams. Data points are mean values from 52 cells and the shaded areas indicate mean ± s.e. determined by bootstrapping. The grey dashed line (bottom right) indicates a time delay of 1 min between a force burst and the thinning of the cell minor axis. **e**, Bright-field (top) and differential interference contrast (bottom) images showing morphological changes of NK cells during migration through collagen pores. The purple arrows highlight immune cells squeezing through dense collagen pores. The cell in the top row is the same as in **a**–**c**, and the white arrows in the bottom row indicate the local matrix deformations between consecutive images.

A disadvantage is that balancing forces from sources outside the image stack can occur throughout the reconstructed force field.

In our Python-based implementation (Saenopy), we regularize the reconstructed forces only within the reconstruction volume but not at its boundaries. This ensures that balancing forces from sources outside the image stack appear only at the surface of the reconstruction volume. Therefore, we do not need to limit the reconstructed cell forces to be within a defined distance around the cell[12,26] (Fig. 1a, middle) and instead can integrate them over the entire reconstruction volume, excluding the surface (Fig. 1a, bottom). This allows the size of the imaged volume to be greatly reduced while retaining high accuracy even for highly contractile cells (Fig. 1c).

It is also no longer required that force-induced matrix deformations near the image-stack boundary are negligible. Further, we image the cells

https://doi.org/10.1038/s41567-024-02632-8

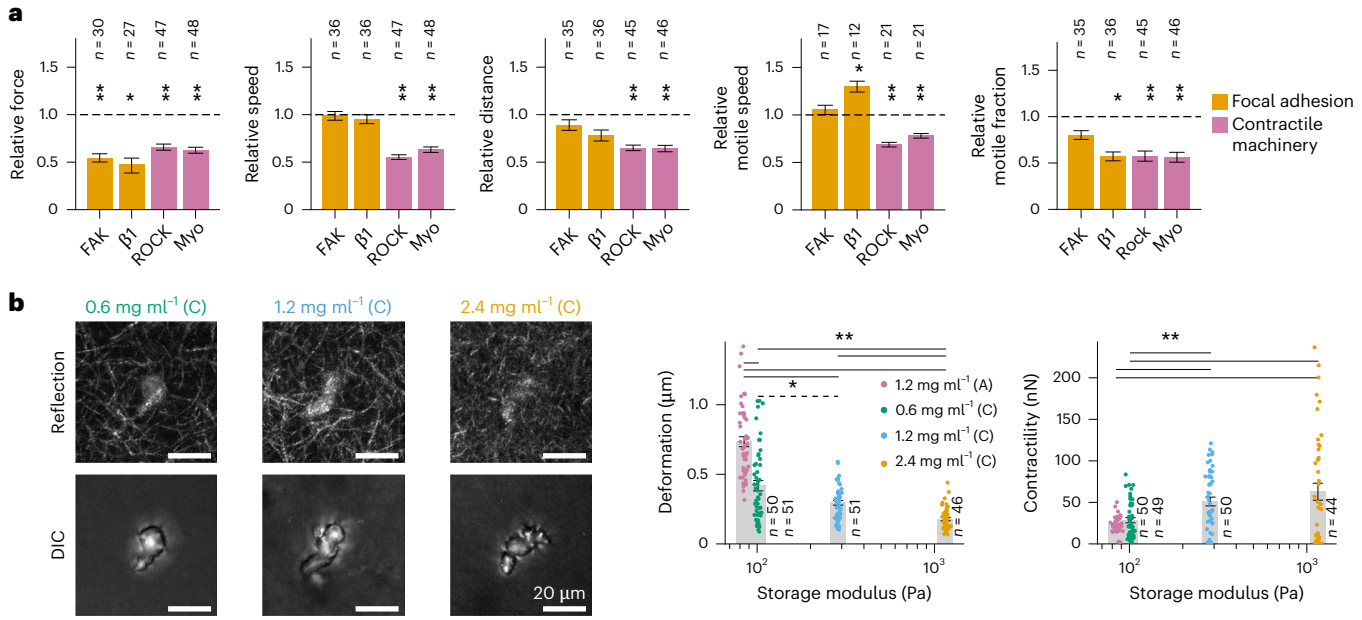

Fig. 3 | Mechanosensing of migrating NK cells in 3D collagen networks. **a**, NK92 cell force measurements during migration in 1.2 mg ml^{-1} collagen gels with inhibition of focal adhesions (FAK and integrin β1 (β1)) or inhibition of the contractile machinery (myosin II (Myo) and Rho kinase (ROCK)). Relative changes of the maximum contractile force, the average cell speed, the cell travelled distance, the average speed of motile cells (overall migration distance >13 µm) and the motile cell fraction are shown in comparison with the mean value of the corresponding control cells (grey dashed line; control cells are treated either with same amount of solvent or isotype controls in the case of antibodies). The error bars indicate mean ± s.e. over all cells from three independent replicates. Error intervals and statistical significance are calculated using bootstrapping; *P < 0.05 and **P < 0.01. N indicates the number of analysed cells (see Methods and Supplementary Fig. 2 for absolute values). **b**, NK92 cell force measurements during migration in collagen gels of different concentration (0.6 mg ml^{-1}, 1.2 mg ml^{-1} and 2.4 mg ml^{-1}). Left: confocal reflection and differential interference contrast (DIC) microscopy images of representative cells. Right: cell contractility (maximum value within 23 min measurement period) and matrix deformations of NK92 cells embedded in collagen gels of different stiffness and collagen batches (A and C; Extended Data Fig. 2). The matrix deformations are calculated from the 99% percentile value of the absolute matrix deformation vectors per timestep (1 min). Then we select the maximum value within a 23 min measurement period). The error bars show mean ± s.e. for n individual cells from three (pink and orange) or four (green and blue) independent experiments. *P < 0.05 and **P < 0.01 for a two-sided t-test with Bonferroni correction[51]. The storage modulus of different collagen gels in the linear regime is derived from shear rheological measurements with 1% strain amplitude and and a frequency of 0.02 Hz (Extended Data Fig. 3). Pore diameter ranges from 5.7 µm (0.6 mg ml^{-1}, batch A) to 3.5 µm (2.4 mg ml^{-1}, batch A; Extended Data Fig. 4).

for a sufficiently long time so that the cell has either migrated outside the image stack or that the cell forces have changed their direction and magnitude multiple times so that the time average (median) of the matrix deformations corresponds to the undeformed state (Fig. 1b, bottom).

From simulations of force-generating dipoles or quadrupoles with cell-like dimensions (15–30 µm) and forces, we verify the linearity of our method over a large force range (2–400 nN) even for highly nonlinear matrices such as collagen (Fig. 1d), and confirm high sensitivity even in the presence of considerable imaging noise. For example, for a simulated cell that generates 20 nN (dipole) or 40 nN (quadrupole) of force, the typical displacement noise level of a confocal microscope of around 100 nm (σ_x = 41 nm, σ_y = 42 nm, σ_z = 99 nm) results in relative errors of contractility below 5% and relative errors of strain energy below 15% (Fig. 1e).

Forces during immune cell migration

The ability to obtain the force-free reference state without killing or relaxing the cells, combined with the ability to recover the traction field from an incomplete deformation field, allows us to measure the dynamic force generation of natural killer (NK) cells (NK92 cell line) during migration in 1.2 mg ml^{-1} collagen gels (shear modulus in the linear range of 100 Pa (Extended Data Figs. 2 and 3), average pore size 4.4 µm (Extended Data Fig. 4 and Supplementary Video 1)). We record one image stack (123 × 123 × 123 µm, voxel size 0.24 × 0.24 × 1 µm, acquisition time of 10 s using a resonance scanner (8,000 Hz) and a galvo stage) every minute for 23 min. From these 23 image-stack pairs, we compute the differential deformations using particle image velocimetry (PIV)[27], integrate them over time and estimate the force-free matrix configuration (undeformed reference state) from the median deformation (Fig. 1b). Cell forces at each time point are then computed from the current matrix deformations relative to the undeformed reference state. This approach for estimating the force-free matrix configuration allows for dynamic deformation measurements of highly motile cells with rapidly fluctuating traction forces and is easily adaptable to existing TFM methods. From the cell positions and cell shapes, we also extract cell velocity and aspect ratio (Fig. 2a,b).

Around 80% of NK cells that are elongated at t = 0 migrate by more than 1 cell diameter (13 µm) during the observation time of 23 min (Supplementary Fig. 1). When migrating, NK cells typically show an elongated morphology, whereas non-migrating cells remain round. The majority of migrating cells show bursts of substantial contractile forces between 5 nN and 50 nN (Fig. 2c and Supplementary Videos 2–8), lasting typically 3–5 min, followed by non-contractile phases (<5 nN). After a contractile phase, the matrix fibres relax to their initial position, indicating predominantly elastic behaviour with no substantial plastic deformations (Supplementary Video 9). Cells migrate both during contractile and non-contractile phases, but contractile phases are significantly (P < 0.01) correlated with higher speed and higher cell aspect ratio (Fig. 2b,c). Accordingly, speed and aspect ratio are also positively correlated (Fig. 2d). Myosin inhibition and Rho-kinase inhibition markedly reduce the magnitude and frequency of force bursts (Fig. 2c) and also reduce the migration speed (Fig. 2c).

Our discovery of substantial contractile forces in migrating immune cells that are approaching or even matching those of much larger cells, such as metastatic breast carcinoma cells (MDA-MB-231) or mouse embryonic fibroblasts[12,28,29], is surprising, as amoeboid migration

https://doi.org/10.1038/s41567-024-02632-8

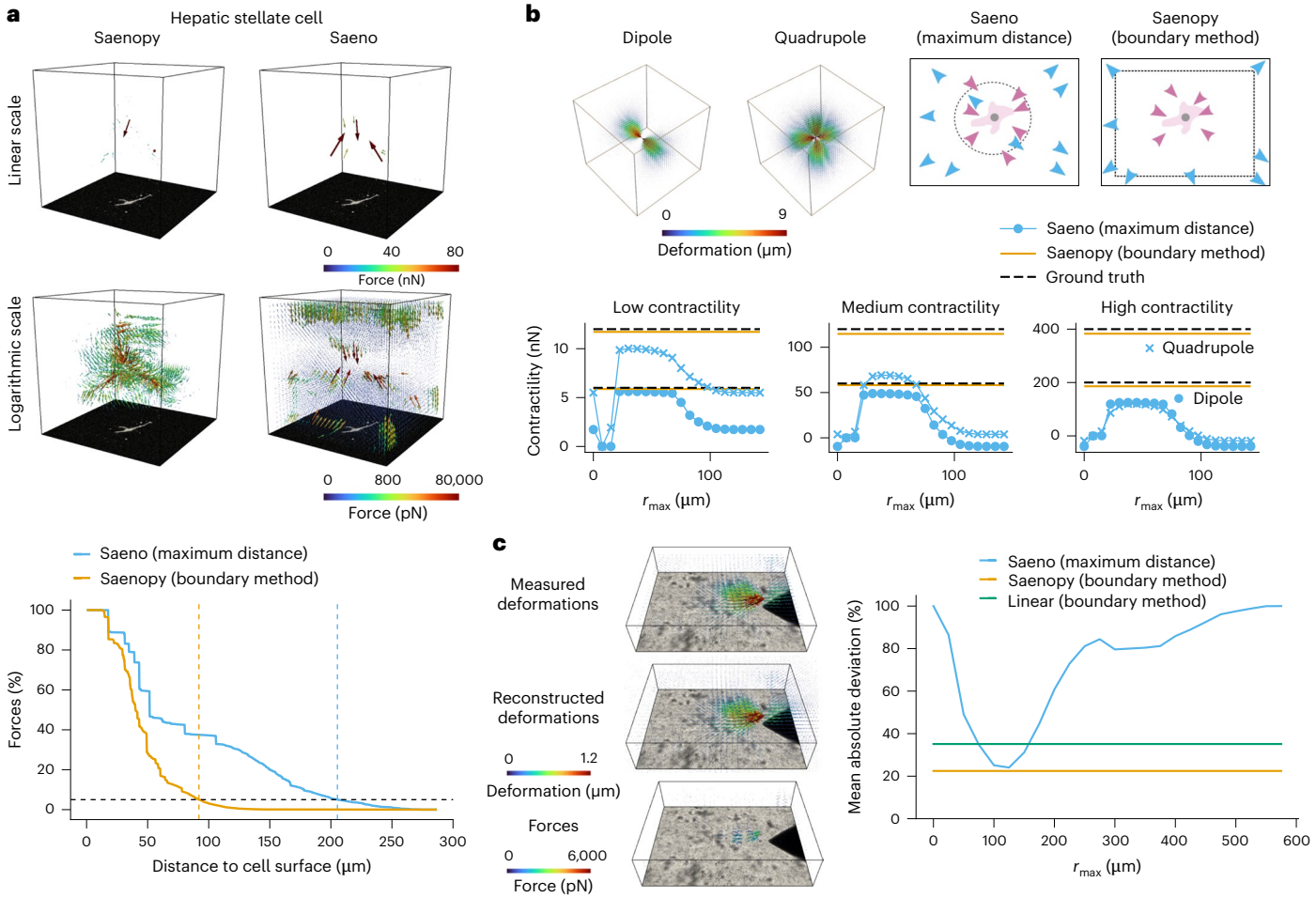

Fig. 4 | Force reconstruction benchmark tests. a, Top: force fields around a hepatic stellate cell embedded for 2 days in 1.2 mg ml^{-1} collagen gels. Forces are reconstructed using Saenopy (boundary method) or Saeno (maximum distance method). Saenopy regularizes forces only in the bulk but not at the boundary, which greatly improves force localization. Bottom: force distribution versus distance to cell surface. The dashed lines indicate the distances from the cell surface covering 95% of all forces. **b**, Benchmark tests comparing the accuracy of force reconstruction using Saenopy (boundary method) and Saeno (maximum distance method). Top left: contractile cells are simulated using dipole or quadrupole forces. The simulated deformation fields are used as an input for force reconstruction. Top right: Saeno reconstructs forces by global regularization and considers forces within a distance (r_{max}, dotted grey line) as cell-generated forces (purple), otherwise as balancing forces (blue). Saenopy reconstructs forces by global regularization except for the boundary regions, ensuring that balancing forces appear only at the boundaries. Bottom: reconstructed contractilities for dipoles (circles) and quadrupoles (crosses) with low (6 nN and 12 nN), medium (60 nN and 120 nN) and high (200 nN and 400 nN) contractility versus maximum distance parameter r_{max} for Saeno (blue solid lines). For comparison, forces reconstructed using Saenopy (orange solid lines) and ground-truth forces (black dashed lines) are shown as horizontal lines. Compared with Saeno, forces reconstructed with Saenopy remain accurate regardless of contractility. **c**, Experimental verification of the force reconstitution method using magnetic tweezer experiments where forces between 8 nN and 23 nN are applied to magnetic microbeads embedded in collagen ($n = 14$) Data from ref. 12. Left: measured deformation field (top), reconstructed deformation field (middle) and reconstructed force field (bottom) within a 433 × 433 × 100 µm volume around a magnetic bead. The tweezer needle is visible in the bright-field image projected below the force and deformation fields. Right: forces are reconstructed using Saenopy (boundary method, orange), Saenopy assuming purely elastic material behaviour (boundary method, green) and Saeno (maximum distance) for different r_{max} (blue). The curves show the magnitude of the difference between the known applied forces and the recovered forces, normalized to the applied forces.

is thought to be facilitated by shape changes and low frictional (traction) forces with the matrix[19,20,30]. While our observation of long migratory phases with low tractions is in agreement with this notion, the occurrence of large traction force bursts points to a strong coupling of the cell's contractile machinery to the extracellular matrix during these brief phases. Such strong coupling may facilitate the migration through small matrix pores that pose a high steric hindrance and require large cell shape changes (Fig. 2e and Supplementary Videos 2–8). In line with this hypothesis, we observe that contractile phases occur when cells migrate through narrow collagen pores (Fig. 2d,e). We find that contractile force bursts are followed by a thinning of the cell minor axis (normalized to cell size; Fig. 2d) with a time delay of 1 min, suggesting that traction forces help NK cells to migrate through narrow pores in the matrix. Similar behaviour has also been confirmed in other immune cell types[31].

To test whether the forces are mediated by focal adhesions and integrins, as in mesenchymally migrating cells, we inhibited focal adhesion kinase (FAK) and integrin β1. Both interventions reduce contractile forces, demonstrating that force transmission is mediated by integrin-based cell–matrix adhesions (Fig. 3a and Supplementary Fig. 2). Interestingly, blocking adhesions reduces the number of motile cells but increases their migration speed (Fig. 3a and Supplementary Fig. 2). Reduced numbers of motile NK cells were also observed in non-adhesive carbomer hydrogels and after the addition of ethylenediamine tetraacetic acid (EDTA) or pluronic, both of which reduce cell–matrix adhesion[31]. These findings suggest that NK

https://doi.org/10.1038/s41567-024-02632-8

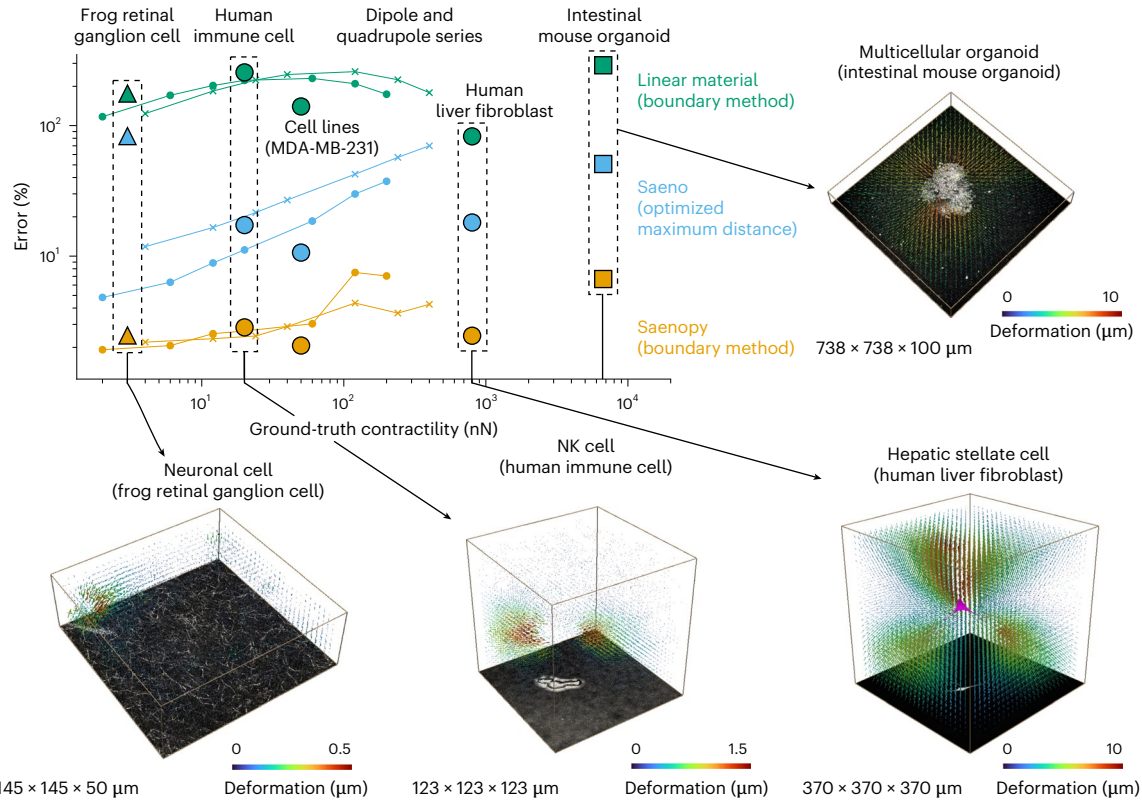

Fig. 5 | Accuracy and broad applicability of Saenopy. The graph shows the relative error of different traction force reconstruction methods for simulated cells or organoids. Cells are simulated as monopoles (large triangles), dipoles (small and large circles) and quadrupoles (small crosses); organoids are simulated as dodecahedra (large rectangles). The magnitudes of simulated forces (indicated by the ground-truth contractility), distances between force monopoles and the size of the simulated deformation field that is used as input for force reconstruction are based on representative experimental data shown adjacent to the graph. Three-dimensional plots show the measured matrix deformation fields (coloured arrows) of different cell types (neurons, immune cells, liver fibroblasts) or cell aggregates (organoids). In addition, force dipoles and quadrupoles with a distance between the force monopoles of 30 µm are simulated for forces between 2 nN and 400 nN (small circles and crosses connected by lines). Force reconstruction is performed using linear Saenopy (boundary method, linear elastic material model without the nonlinear material parameters buckling coefficient d_0, characteristic strain λ_s and stiffening coefficient d_s; green), nonlinear Saeno (maximum distance r_{max} is optimized for highest possible accuracy; blue) and nonlinear Saenopy (boundary method; orange).

cells migrate preferentially in an amoeboid manner, but to overcome narrow pores, they can form integrin-mediated matrix adhesions and generate substantial traction forces. As expected, impairing the contractile machinery by inhibition of Rho kinase or myosin reduces both cellular forces and the migration speed (Fig. 3a and Supplementary Fig. 2).

Our finding of a strong coupling between the contractile machinery of immune cells and the mechanical properties of the extracellular matrix is supported by our finding of increasing tractions in collagen gels with increasing stiffness (Fig. 3b and Extended Data Fig. 5). This behaviour is reminiscent of mesenchymal cells that typically also respond with higher traction forces to higher matrix stiffness[18,32,33]. In mesenchymal cells, this mechano-sensitive behaviour is facilitated by integrin-mediated cell adhesions with the matrix. Our findings of a similar mechano-sensitive behaviour in immune cells, together with our discovery large traction force bursts, suggest that strong integrin-mediated adhesions may also be involved in immune cell migration through tight constrictions. This finding may have broad biological implications and adds to our current understanding of how immune cells migrate through tissue for their homing towards target sites in inflammation or cancer.

Force measurements across spatial and temporal scales

Importantly, by regularizing the reconstructed forces only within the reconstruction volume and not at its boundaries, our method improves force localization. In particular, reconstructed cell forces are located closer to the cell surface, and balancing forces and forces originating from sources outside the imaged volume are located at the boundary of the imaged volume. This greatly simplifies the analysis compared with previous methods, as the maximum distance parameter (r_{max}) that separates cell-generated forces from balancing forces is no longer required. This is particularly important for large traction forces where the maximum distance approach has increasing difficulty in distinguishing between cell-generated and balancing forces, whereas our method remains accurate even when the imaged volume is greatly reduced (Fig. 1c and Supplementary Fig. 3). We further validate the method using magnetic tweezer experiments, where we can accurately recover the forces applied to magnetic microbeads embedded in collagen, whereas the maximum distance approach provides accurate force estimates only for a narrow range of the r_{max} parameter (Fig. 4c).

In the following, we exploit the ability of our method to reconstruct traction forces over four orders of magnitude, demonstrating its broad applicability to a wide range of single-cell and multicellular systems. We first apply our method to measure traction forces of growth cones from retinal ganglion cell axons of African clawed frogs (*Xenopus laevis*). From two-dimensional TFM measurements, it is known that forces of axonal growth cones are small (1–10 nN)[34–36] and highly dynamic[36,37]. In 3D collagen and polyethylene glycol (PEG) gels, axons' growth cones have been reported to generate no measurable traction forces[38]. As axons are typically much larger than the 145 µm size of our image stacks, traction forces can be partially unbalanced. Our method overcomes

these challenges and resolves traction forces of axonal growth cones in three dimensions of around 3 nN. Similar to the behaviour of immune cells, these forces act only intermittently and longer periods of axon growth can occur without detectable traction forces (Extended Data Fig. 6 and Supplementary Video 10).

Next, to test our method at the other end of the force range where traction forces are so large that they induce nonlinear responses in the surrounding matrix, we measure primary liver fibroblasts (human hepatic stellate cells) as well as 100-µm-sized multicellular mouse intestinal organoids (Extended Data Fig. 6 and Supplementary Videos 11 and 12). Such large traction forces are fundamentally important, for example, in wound healing[39,40], fibrosis[41] and cancer[42,43]. Even more extensive matrix deformations are seen around multicellular spheroids or organoids that typically consist of hundreds or thousands of cells and can serve as more complex biological model systems[44–49]. In all these cases, matrix deformations are large (~10 µm) and reach beyond the size of the image stacks. Nonetheless, cell-generated forces (~0.5–10 µN) are reconstructed with high sensitivity (Fig. 5) near the cell or organoid surface (Extended Data Fig. 6). Due to the strong material nonlinearity, large matrix deformations around spheroids and organoids can lead to slow convergence of the force reconstruction algorithm. Our method takes advantage of the fact that the relative changes of the deformations and tractions between two consecutive time points are usually small. Therefore, we can use the deformation field from the preceding time point as the starting configuration for the force reconstruction of the subsequent time point. In the case of organoids, this approach speeds up the convergence of the algorithm by a factor of 5–50.

In summary, our method allows for the dynamic measurement of small to large 3D traction forces over prolonged time periods in linear or nonlinear 3D fibre networks such as collagen, Matrigel or fibrin. The method shows increased sensitivity and accuracy compared with previous 3D TFM methods (Figs. 4 and 5, and Supplementary Figs. 3–5), requires only a small confocal or bright-field image stack (Extended Data Figs. 6 and 7, Supplementary Fig. 6 and Supplementary Video 13), and is insensitive to forces from sources outside the imaged volume (Fig. 1c and Supplementary Fig. 3). The method can be applied to single cells, cell colonies, spheroids and organoids. For a user-friendly implementation of the method, we provide a Python-based open-source software platform[50] with a graphical user interface (Supplementary Figs. 7 and 8).

Online content

Any methods, additional references, Nature Portfolio reporting summaries, source data, extended data, supplementary information, acknowledgements, peer review information; details of author contributions and competing interests; and statements of data and code availability are available at https://doi.org/10.1038/s41567-024-02632-8.

References

1. Dembo, M. & Wang, Y. L. Stresses at the cell-to-substrate interface during locomotion of fibroblasts. *Biophys. J.* **76**, 2307–2316 (1999).
2. Han, S. J., Oak, Y., Groisman, A. & Danuser, G. Traction microscopy to identify force modulation in subresolution adhesions. *Nat. Methods* **12**, 653–656 (2015).
3. Huang, Y. et al. Traction force microscopy with optimized regularization and automated Bayesian parameter selection for comparing cells. *Sci. Rep.* **9**, 539 (2019).
4. Butler, J. P., Tolic-Norrelykke, I. M., Fabry, B. & Fredberg, J. J. Traction fields, moments, and strain energy that cells exert on their surroundings. *Am. J. Physiol. Cell Physiol.* **282**, C595–C605 (2002).
5. Bergert, M. et al. Confocal reference free traction force microscopy. *Nat. Commun.* **7**, 12814 (2016).
6. Sabass, B., Gardel, M. L., Waterman, C. M. & Schwarz, U. S. High resolution traction force microscopy based on experimental and computational advances. *Biophys. J.* **94**, 207–220 (2008).
7. Bauer, A. et al. pyTFM: a tool for traction force and monolayer stress microscopy. *PLoS Comput. Biol.* **17**, e1008364 (2021).
8. Gómez-González, M., Latorre, E., Arroyo, M. & Trepat, X. Measuring mechanical stress in living tissues. *Nat. Rev. Phys.* **2**, 300–317 (2020).
9. Barrasa-Fano, J. et al. TFMLAB: a MATLAB toolbox for 4D traction force microscopy. *SoftwareX* **15**, 100723 (2021).
10. Legant, W. R. et al. Measurement of mechanical tractions exerted by cells in three-dimensional matrices. *Nat. Methods* **7**, 969–971 (2010).
11. Franck, C., Maskarinec, S. A., Tirrell, D. A. & Ravichandran, G. Three-dimensional traction force microscopy: a new tool for quantifying cell–matrix interactions. *PLoS ONE* **6**, e17833 (2011).
12. Steinwachs, J. et al. Three-dimensional force microscopy of cells in biopolymer networks. *Nat. Methods* **13**, 171–176 (2016).
13. Song, D. et al. Recovery of tractions exerted by single cells in three-dimensional nonlinear matrices. *J. Biomech. Eng.* **142**, 081012 (2020).
14. Dong, L. & Oberai, A. A. Recovery of cellular traction in three-dimensional nonlinear hyperelastic matrices. *Comput. Methods Appl. Mech. Eng.* **314**, 296–313 (2017).
15. Toyjanova, J. et al. High resolution, large deformation 3D traction force microscopy. *PLoS ONE* **9**, e90976 (2014).
16. Storm, C., Pastore, J. F., MacKintosh, F. C., Lubensky, T. C. & Janmey, P. A. Nonlinear elasticity in biological gels. *Nature* **435**, 188–191 (2005).
17. Munster, S. et al. Strain history dependence of the nonlinear stress response of fibrin and collagen networks. *Proc. Natl Acad. Sci. USA* **110**, 12197–12202 (2013).
18. Discher, D. E., Janmey, P. & Wang, Y. L. Tissue cells feel and respond to the stiffness of their substrate. *Science* **310**, 1139–1143 (2005).
19. Friedl, P., Noble, P. B. & Zänker, K. S. T lymphocyte locomotion in a three-dimensional collagen matrix. Expression and function of cell adhesion molecules. *J. Immunol.* **154**, 4973–4985 (1995).
20. Friedl, P., Entschladen, F., Conrad, C., Niggemann, B. & Zänker, K. S. $CD4^+$ T lymphocytes migrating in three-dimensional collagen lattices lack focal adhesions and utilize β1 integrin-independent strategies for polarization, interaction with collagen fibers and locomotion. *Eur. J. Immunol.* **28**, 2331–2343 (1998).
21. Yamada, K. M. & Sixt, M. Mechanisms of 3D cell migration. *Nat. Rev. Mol. Cell Biol.* **20**, 738–752 (2019).
22. Caillier, A., Oleksyn, D., Fowell, D. J., Miller, J. & Oakes, P. W. T cells use focal adhesions to pull themselves through confined environments. *J. Cell Biol.* **223**, e202310067 (2024).
23. Kaltenbach, L. & Lämmermann, T. Mast cell migration and organization in tissues depend on integrin–ECM interactions. *Nat. Immunol.* **24**, 899–900 (2023).
24. François, J. et al. The interplay between matrix deformation and the coordination of turning events governs directed neutrophil migration in 3D matrices. *Sci. Adv.* **7**, eabf3882 (2021).
25. Huse, M. Mechanical forces in the immune system. *Nat. Rev. Immunol.* **17**, 679–690 (2017).
26. Cóndor, M., Steinwachs, J., Mark, C., García-Aznar, J. M. & Fabry, B. Traction force microscopy in 3-dimensional extracellular matrix networks. *Curr. Protoc. Cell Biol.* **75**, 10.22.1–10.22.20 (2017).
27. Liberzon, A., Käufer, T., Bauer, A., Vennemann, P. & Zimmer, E. OpenPIV/openpiv-python: OpenPIV-Python v0.23.4. *Zenodo* https://doi.org/10.5281/zenodo.4409178 (2021).
28. Thievessen, I. et al. Vinculin is required for cell polarization, migration, and extracellular matrix remodeling in 3D collagen. *FASEB J.* **29**, 4555–4567 (2015).
29. Cóndor, M. et al. Breast cancer cells adapt contractile forces to overcome steric hindrance. *Biophys. J.* **116**, 1305–1312 (2019).

30. Wolf, K., Müller, R., Borgmann, S., Bröcker, E. B. & Friedl, P. Amoeboid shape change and contact guidance: T-lymphocyte crawling through fibrillar collagen is independent of matrix remodeling by MMPs and other proteases. *Blood* **102**, 3262–3269 (2003).
31. Czerwinski, T. et al. Immune cells employ intermittent integrin-mediated traction forces for 3D migration. Preprint at *bioRxiv* https://doi.org/10.1101/2023.04.20.537658 (2023).
32. Reinhart-King, C. A., Dembo, M. & Hammer, D. A. Cell–cell mechanical communication through compliant substrates. *Biophys. J.* **95**, 6044–6051 (2008).
33. Paszek, M. J. et al. Tensional homeostasis and the malignant phenotype. *Cancer Cell* **8**, 241–254 (2005).
34. Heidemann, S. R., Lamoureux, P. & Buxbaum, R. E. Growth cone behavior and production of traction force. *J. Cell Biol.* **111**, 1949–1957 (1990).
35. Betz, T., Koch, D., Lu, Y. B., Franze, K. & Käs, J. A. Growth cones as soft and weak force generators. *Proc. Natl Acad. Sci. USA* **108**, 13420–13425 (2011).
36. Koch, D., Rosoff, W. J., Jiang, J., Geller, H. M. & Urbach, J. S. Strength in the periphery: growth cone biomechanics and substrate rigidity response in peripheral and central nervous system neurons. *Biophys. J.* **102**, 452–460 (2012).
37. Polackwich, R. J., Koch, D., McAllister, R., Geller, H. M. & Urbach, J. S. Traction force and tension fluctuations in growing axons. *Front. Cell. Neurosci.* **9**, 417 (2015).
38. Santos, T. E. et al. Axon growth of CNS neurons in three dimensions is amoeboid and independent of adhesions. *Cell Rep.* **32**, 107907 (2020).
39. Singer, A. J. & Clark, R. A. Cutaneous wound healing. *N. Engl. J. Med.* **341**, 738–746 (1999).
40. Li, B. & Wang, J. H. Fibroblasts and myofibroblasts in wound healing: force generation and measurement. *J. Tissue Viability* **20**, 108–120 (2011).
41. Kang, N. Mechanotransduction in liver diseases. *Semin. Liver Dis.* **40**, 84–90 (2020).
42. Joyce, J. A. & Pollard, J. W. Microenvironmental regulation of metastasis. *Nat. Rev. Cancer* **9**, 239–252 (2009).
43. Calvo, F. et al. Mechanotransduction and YAP-dependent matrix remodelling is required for the generation and maintenance of cancer-associated fibroblasts. *Nat. Cell Biol.* **15**, 637–646 (2013).
44. Sato, T. et al. Long-term expansion of epithelial organoids from human colon, adenoma, adenocarcinoma, and Barrett's epithelium. *Gastroenterology* **141**, 1762–1772 (2011).
45. Eiraku, M. et al. Self-organizing optic-cup morphogenesis in three-dimensional culture. *Nature* **472**, 51–58 (2011).
46. Lancaster, M. A. et al. Cerebral organoids model human brain development and microcephaly. *Nature* **501**, 373–379 (2013).
47. Gjorevski, N. et al. Tissue geometry drives deterministic organoid patterning. *Science* **375**, eaaw9021 (2022).
48. Pérez-González, C. et al. Mechanical compartmentalization of the intestinal organoid enables crypt folding and collective cell migration. *Nat. Cell Biol.* **23**, 745–757 (2021).
49. Poling, H. M. et al. Mechanically induced development and maturation of human intestinal organoids in vivo. *Nat. Biomed. Eng.* **2**, 429–442 (2018).
50. Gerum, R., Böhringer, D. & Cóndor, M. Saenopy Github Project. *GitHub* https://github.com/rgerum/saenopy (2020).
51. Bonferroni, C. E. *Teoria Statistica Delle Classi e Calcolo Delle Probabilità* (Florence R. Istituto Superiore di Scienze Economiche e Commerciali, 1936).

[1]Department of Physics, Friedrich-Alexander-Universität Erlangen-Nürnberg, Erlangen, Germany. [2]Life Sciences Technology Department, Interuniversity Micro-Electronics Centre, Leuven, Belgium. [3]Biomechanics Section, Department of Mechanical Engineering, KU Leuven, Leuven, Belgium. [4]Institute of Medical Physics and Microtissue Engineering, Friedrich-Alexander-Universität Erlangen-Nürnberg, Erlangen, Germany. [5]Max-Planck-Zentrum für Physik und Medizin, Erlangen, Germany. [6]Department of Medicine 1, Friedrich-Alexander-Universität Erlangen-Nürnberg, Erlangen, Germany. [7]Deutsches Zentrum Immuntherapie (DZI), Friedrich-Alexander-Universität Erlangen-Nürnberg, Erlangen, Germany. [8]Department of Dermatology, University Hospital Erlangen, Friedrich-Alexander-Universität Erlangen-Nürnberg, Erlangen, Germany. [9]Department of Physiology, Development and Neuroscience, University of Cambridge, Cambridge, UK. [10]Institute of Continuum Mechanics and Biomechanics, Friedrich-Alexander-Universität Erlangen-Nürnberg, Erlangen, Germany. [11]Department of Physics and Astronomy, York University, Toronto, Ontario, Canada. ✉e-mail: ben.fabry@fau.de

Methods

Material model

Our method uses a previously developed material model for biopolymer hydrogels[12,52]. The material is filled with isotropically oriented fibres, each exhibiting the same nonlinear stiffness (ω'') versus strain (λ) relationship according to equation (1) (Extended Data Fig. 1). In particular, for small extensional strain in the linear range ($0 < \lambda < \lambda_s$), fibres exhibit a constant stiffness k. For compressive strain ($-1 < \lambda < 0$), fibres buckle and show an exponential decay of the stiffness with a characteristic buckling coefficient d_0. For larger extensional strain beyond the linear range ($\lambda_s < \lambda$), the fibres show strain stiffening with an exponential increase of stiffness with a characteristic stiffening coefficient d_s. See (Extended Data Fig. 1) for a schematic of the material model.

$$w''(\lambda) = \begin{cases} k \exp\left(\frac{\lambda}{d_0}\right) & \text{if } -1 \le \lambda < 0 \text{ softening} \\ k & \text{if } 0 \le \lambda < \lambda_s \text{ linear} \\ k \exp\left(\frac{\lambda - \lambda_s}{d_s}\right) & \text{if } \lambda_s \le \lambda \text{ stiffening} \end{cases} \quad (1)$$

This description gives rise to a semi-affine behaviour: macroscopic material deformations cause non-affine deformations of the individual fibres, for example, some fibres may buckle while others are stretched, depending on their orientation. Using a mean-field approach, we approximate the material behaviour by averaging over many isotropically oriented fibres so that all spatial directions contribute equally.

Specifically, the energy function $w(\lambda)$ is used to calculate the energy density W stored in the material for a given deformation gradient $\mathbf{F}$, averaged over the full solid angle Ω (refs. 12,52):

$$W = \langle \omega(|\mathbf{F} \cdot \mathbf{e}_r(\Omega)| - 1) \rangle_\Omega \quad (2)$$

The strain λ of a unit vector $\mathbf{e}_r(\Omega)$ (representing a fibre), $\lambda = |\mathbf{F} \cdot \mathbf{e}_r(\Omega)| - 1$, is used to calculate the energy $\omega(\lambda)$ stored in this spatial direction. The strain is averaged over the full solid angle Ω, approximated by a finite set (typically 300) of homogeneously and isotropically distributed unit vectors $\mathbf{e}_r(\Omega)$.

Finite-element model

To describe the material behaviour in the case of an inhomogeneous deformation field, we tessellate the material volume into a mesh of linear tetrahedral elements T. The deformation field is then modelled as deformations $\mathbf{U}$ of the nodes of these elements. The total energy $E(\mathbf{U})$ of the mesh is the sum over the energy density W of all tetrahedral elements T multiplied by their volume V_T:

$$E(\mathbf{U}) = \sum_T W(\mathbf{F}(\mathbf{U})_T) \cdot V_T \quad (3)$$

From the total energy $E(\mathbf{U})$, we calculate the stiffness matrix $K(\mathbf{U})$ and the nodal forces $\mathbf{f}(\mathbf{U})$ (refs. 12,52):

$$K_{ij}(\mathbf{U}) = \frac{\partial E(\mathbf{U})}{\partial \mathbf{U}_i \partial \mathbf{U}_j} \quad (4)$$

$$\mathbf{f}_i(\mathbf{U}) = \frac{\partial E(\mathbf{U})}{\partial \mathbf{U}_i} \quad (5)$$

Index i represents the nodes of the finite-element mesh and index j represents the adjacent nodes.

Mechanical characterization of biopolymer networks

We investigated the influence of three different collagen batches (A, B and C) and different collagen concentrations (0.6 mg ml^{-1}, 1.2 mg ml^{-1} and 2.4 mg ml^{-1}) on the material behaviour and the resulting material model parameters (Extended Data Fig. 2). Two different rheological experiments were performed to measure the macro-rheological behaviour of collagen hydrogels. First, we used a cone-plate rheometer (Discovery HR-3, TA Instruments, 20 mm cone-plate geometry, 2° angle, truncation gap 54 µm) to measure the stress–strain relationship of collagen gels for simple shear deformation. The collagen sample (85 µl) was polymerized inside the rheometer set-up at 37 °C for 30 min. A solvent trap filled with water was used to prevent evaporation and drying out of the sample. An initial frequency sweep (0.2–2 Hz) was performed at a low amplitude of 1%. Then, the stress–strain relationship was measured for a strain ramp from 0% to 100% with a constant strain rate of 1% s^{-1}.

In a second experiment, we measured the vertical contraction of collagen gels in response to horizontal uniaxial stretching. Stretching was performed using 2 × 2 cm flexible polydimethylsiloxane (PDMS) membranes (Sylgard 184; crosslinker-to-base ratios of 1:14; cured for 24 h at 65 °C, Sigma-Aldrich) as described in ref. 53. The PDMS membrane was pre-stretched to 5% and coated with 0.5 mg ml^{-1} sulfo-SANPAH (Thermo Fisher Scientific) followed by 5 min ultraviolet treatment and washing 3 times with phosphate buffered saline (Gibco PBS, Thermo Fisher Scientific). Next, 700 µl of unpolymerized collagen solution was mixed with 4 µm silica beads (Kisker Biotech) that served as fiducial markers (5 µl beads per 1 ml). The collagen solution was transferred to the PDMS membrane, and after 20 min polymerization at 37 °C and 5% CO_2, another 5 µl of the silica bead suspension was pipetted onto the gel to mark the gel surface. The collagen was polymerized for a total of 1 h, after which 1 ml DMEM medium (1 g l^{-1} glucose, Thermo Fisher Scientific) was added on top. The collagen gel was stretched uniaxially in 1% step increments using a custom-made stepper motor-driven cell-stretching device[54] mounted on an epifluorescence microscope (Leica DMI6000 CS equipped with a ×20 Leica HCX PL Fluotator objective, Leica). For each stretch increment, we measured the gel thickness by focusing on the top and bottom surface of the gel (highest and lowest layer of beads) and correct for the refractive index of water.

For collagen batch D (used only for axon growth cone measurements), the stress–strain relationship was determined using a rheometer equipped with a 25-mm-diameter cone-plate geometry (MCR302e, AntonPaar). The polymerization of 50 µl hydrogel between the rheometer plates was monitored for 90 min at 20 °C using an oscillatory strain of 0.5%. After polymerization, a frequency sweep (0.1–100 rad s^{-1}) with 0.5% strain was performed, followed by a strain ramp at a constant strain rate of 0.5% s^{-1} (Supplementary Fig. 9).

As a cone-plate rheometer or uniaxial stretching device may not be available in every laboratory, and hence the correct material parameter for a given collagen batch may be unknown, we also quantified the effects of using erroneous material parameters on cellular force reconstruction (Supplementary Figs. 10–12). Furthermore, we explored the possibility to derive the linear stiffness parameter k_0 of the material model, which most sensitively affects force reconstruction, from oscillatory cone-plate rheology measurements in the linear range (Extended Data Fig. 3).

Estimating material parameters from rheological measurements

As the material model is based on the mechanical behaviour of microscopic biopolymer fibres, the model parameters cannot be directly extracted from macroscopic rheological measurements. Instead, we simulated the macro-rheological experiments using different model parameters until a best fit was achieved (Extended Data Fig. 2). Data from uniaxial stretching are required to fit the buckling coefficient d_0 of the material. For the other parameters, data from either a shear rheometry or an extensional rheometry experiment are sufficient as long as the strain range exceeds the linear range of the material[50].

Collagen gel preparation

Collagen type 1 hydrogels were prepared from acid-dissolved rat tail (R) and bovine skin (G1) collagen (Matrix Bioscience). Both collagen types were mixed ice-cold at a mass ratio of 1:2 and were dissolved in a dilution medium containing 1 vol. part $NaHCO_3$, 1 vol. part 10× DMEM and 8 vol. parts H_2O, adjusted to pH 9 using NaOH. The final collagen concentrations were adjusted to 0.6 mg ml^{-1}, 1.2 mg ml^{-1} or 2.4 mg ml^{-1} using dilution medium. The the final mixture was then adjusted to pH 9 using NaOH. Collagen gels were polymerized for 1 h at 5% CO_2 and 37 °C.

For axon growth cone measurements, collagen type 1 hydrogels were prepared from acid-dissolved bovine collagen (TeloCol-10, Advanced Biomatrix). Six parts Leibovitz L-15 medium (Gibco, Thermo Fisher Scientific), 3 parts autoclaved double-distilled water and 1 part collagen solution were prepared for a final collagen concentration of 1 mg ml^{-1}. HEPES buffer (15 mM, Sigma-Aldrich), 100 units per ml penicillin-streptomycin and 0.25 µg ml^{-1} amphotericin B (Lonza) were added, and the final mixture was adjusted to pH 7.3 using NaOH. Collagen gels were polymerized for 1 h at ambient CO_2 and 20 °C.

Cell culture and 3D traction force experiments

Immune cells. NK92 cells (ATCC CRL-2407) were cultured at 37 °C and 5% CO_2 in alpha-MEM medium (Stemcell Technologies) with 15% fetal calf serum, 15% horse serum, 500 IU ml^{-1} human IL2-cytokine and 1% penicillin-streptomycin solution (10.000 units per ml penicillin, 10.000 µg ml^{-1} streptomcycin). Cells were suspended in 3 ml ice-cold collagen (1.2 mg ml^{-1}) solution (66.000 cells per ml), transferred to a 35 mm Nunc dish (Thermo Fisher Scientific) and polymerized at 37 °C, 5% CO_2 for 1 h. After polymerization, 2 ml of pre-warmed medium was added and the sample was transferred to an upright laser-scanning confocal microscope (Leica SP5, equipped with an environmental chamber to measure at 37 °C, 5% CO_2). To achieve high time resolution, we used a resonance scanner (8,000 Hz) in combination with a galvo stage. Image stacks (123 × 123 × 123 µm with a voxel size of 0.24 × 0.24 × 1 µm) around individual cells were recorded in bright-field and confocal reflection mode using a ×20 water dip-in objective (HCX APO L 20×/1.00 W, Leica). The acquisition time for an individual image stack was below 10 s. Up to 4 individual cells at different positions were recorded every minute over a period of 23 min.

Liver fibroblasts. Human hepatic stellate cells (HUCLS, Lonza) were cultured at 37 °C, 95% humidity and 5% CO_2 in human hepatic stellate cell growth medium (MCST250, Lonza). Three millilitres of collagen solution (1.2 mg ml^{-1}, batch C) was mixed with 35,000 cells and transferred to a 35 mm Petri dish (Greiner AG). Samples were polymerized at 37 °C for 60 min, after which 2 ml of cell culture medium was added. Two days after seeding, the medium was replaced with fresh medium, and cells were stained using 2 µM calcein AM (Thermo Fisher Scientific). Samples were transferred to an upright laser-scanning confocal microscope (Leica SP5) equipped with a ×20 water dip-in objective (HCX APO L 20×/1.00 W, Leica) and an environmental chamber (37 °C with 5% CO_2). Cubic image stacks (370 µm)^3 with a voxel size of 0.72 × 0.72 × 0.99 µm were recorded around the cells in bright-field, fluorescence and confocal reflection mode. The force-free reference state was acquired ~30 min after drug-induced relaxation of cell forces using 10 µM cytochalsin D (Sigma-Aldrich). Force reconstruction was performed on confocal reflection image stacks using an element size of 14 µm for performing PIV, a PIV window size of 35 µm and a signal-to-noise filter of 1.3. The finite-element model had an element size of 14 µm. The regularization parameter α was set to 10^{10} and the material properties for collagen batch C are used Extended Data Fig. 2.

Axon growth cones. *Xenopus* medium was prepared from 6 parts Leibovitz L-15 medium and 4 parts autoclaved double-distilled water, 100 units per ml penicillin-streptomycin and 0.25 µg ml^{-1} amphotericin B (Lonza). Primary eye primordia explants were dissected from *X. laevis* embryos as previously described[55]. In brief, *Xenopus* embryos developed from in vitro fertilized eggs at ambient CO_2 and 20 °C in 0.1× Marc's modified Ringer's solution. After typically 6 days of incubation, embryos at a development stage of 35/36 (ref. 56) were transferred to a PDMS-coated dissection dish (Sylgard 184, Dow) filled with equal parts of MS-222 anaesthetization medium (Sigma-Aldrich) and *Xenopus* medium.

Explants were dissected under a preparation microscope (Leica) under circular movements of dissection pins around the eye to remove the surrounding skin, and shear movements to extract the retinal explants. Dissected eyes were stored for no longer than 1 h in *Xenopus* medium. The retinal explants were suspended in 50 µl *Xenopus* medium, and 1 ml of ice-cold collagen 1.0 mg ml^{-1} solution (batch D) was prepared and mixed gently with the explant-medium solution. To prevent the explants from sinking to the bottom, the mixture was pre-polymerized for approximately 30 s at room temperature before it was transferred to a 35 mm Petri dish (Ibidi). The sample was polymerized for 2.5 h at room temperature, after which 2 ml of *Xenopus* medium was added and the sample was stored at ambient CO_2 and 20 °C. After 29 h, the sample was transferred to a laser-scanning confocal microscope (TCS SP8, Leica) equipped with an oil immersion/objective (HC PL APO 40×/1.30, Leica). Image stacks (145 × 145 × 50 µm with a voxel size of 0.14 × 0.14 × 1 µm) around a developing axon growth cone were recorded in bright-field and confocal reflection mode every 5 min for a duration of 2 h. *Xenopus* experiments were conducted in accordance with the UK Animals (Scientific Procedures) Act 1986.

Force reconstruction was performed on confocal reflection image stacks (Supplementary Video 10) using a PIV element size of 4.8 µm, a PIV window size of 12 µm and a signal-to-noise filter of 1.3. The finite-element model had an element size of 4.8 µm. The regularization parameter α was set to 10^{11}, and the material properties for collagen batch D were used (Supplementary Fig. 9).

Intestinal organoids. Experiments involving mice were approved by the Institutional Animal Care and Use Committee of the University of Erlangen-Nuremberg and by the Government of Mittelfranken (Würzburg, Germany). Small intestines were collected from C57BL/6J mouse (strain number 000664, The Jackson Laboratory), washed with ice-cold PBS and longitudinally opened. Villi were mechanically removed with the help of a glass coverslide, the tissue was then cut into 1 cm pieces and incubated in chelation buffer (2 mM EDTA in PBS) with gentle shaking in a rocking rotator for 1 h. After several washing steps with ice-cold PBS, the supernatant was filtered through a 70 µm cell strainer to collect isolated crypts. They were embedded in basement membrane extract hydrogels (Cultrex RGF, Biotechne) and placed in a pre-warmed 48-well plate (Nunc delta surface, Thermo Fisher Scientific). The organoids were cultured in Advanced DMEM/F12 medium (Gibco, Thermo Fisher Scientific) supplemented with *N*-acetylcistein (1 mM, Sigma-Aldrich), mEGF (50 ng ml^{-1}, ImmunoTools), B27 and N2 supplement (1x, Life Technologies), Primocin (50 µg ml^{-1}, InvivoGen), and conditioned medium from R-spondin1 and mNoggin-producing cells (batch dilution is defined experimentally based on titration using organoid survival as read-out). The medium was changed every 3 days and organoids were passaged every 7–10 days. For collection and passaging, organoids were dissociated and separated from the surrounding matrix by repeated pipetting and centrifugation (300*g* at 4 °C for 5 min).

For traction force measurements, organoids are embedded in 1.2 mg ml^{-1} collagen type I hydrogels (batch C). A two-layered gel was used to prevent sinking of organoids to the bottom during polymerization[57,58]. In brief, 1.5 ml collagen solution was transferred to a 35 mm dish and polymerized for 20 min (5% CO_2, 37 °C). The supernatant medium from the collected organoids was removed, and the organoids were diluted in another 1.5 ml of collagen solution. The mixture was then added on the pre-polymerized collagen layer. After 1 h of polymerization, 2 ml of medium was added. Before imaging, organoids were stained

with 2 µM calcein AM (Thermo Fisher Scientific) and transferred to an upright laser-scanning confocal microscope (Leica SP5, 37 °C, 5% CO_2). Image stacks (738 × 738 × 100 µm with a voxel size of 0.74 × 0.74 × 2 µm) around an organoid were recorded every 20 min in bright-field, fluorescence and confocal reflection mode using a water dip-in objective (HCX APO L 20×/1.00 W, Leica). Organoid-generated forces were relaxed after ~24 h using 10 µM cytochalsin D (Sigma-Aldrich) and 0.1% triton x-100 (Sigma-Aldrich). The force-free reference state was acquired ~2 h later (Supplementary Video 12).

Force reconstruction was performed on confocal reflection image stacks using a PIV element size of 30 µm, a PIV window size of 40 µm and a signal-to-noise filter of 1.3. The finite-element model had dimensions of $(738\ \mu m)^3$ with an element size of 30 µm. The regularization parameter α was set to 10^{10}, and material properties of collagen batch C were used (Extended Data Fig. 2).

Bright-field microscopy

During migration through the collagen network, NK92 cells were imaged in differential interference contrast mode (Leica DMI6000B, with an HC PL APO 63×/1,40 oil immersion objective) with 2 s between consecutive images (Fig. 2e, bottom).

Measurement of matrix deformations

Cell-induced matrix deformations were measured from confocal reflection image stacks of the collagen network using the open-source PIV algorithm OpenPIV[27] that we extended specifically for analysing 3D image stacks. Saenopy offers two options for quantifying matrix deformations. First, matrix deformations can be calculated between a deformed state and a force-free reference state (Fig. 1b, top). The reference image stack is typically recorded after drug-induced force relaxation using, for example, high concentrations of cytochalasin D[12,26,57]. For fast-moving cells, Saenopy offers a second option for obtaining the reference state from a sufficiently long time series of image stacks (Fig. 1b, bottom). First, the change in matrix deformations between consecutive image stacks, which correspond to the time derivative of the matrix deformations, are calculated at each voxel position using OpenPIV[27]. We then calculate the cumulative sum of the time derivative at each voxel, which corresponds to the absolute matrix deformation apart from an offset. To remove the offset, we subtract the median deformation at each voxel position, assuming that the median matrix deformations around a fast-moving cell tend towards zero, when observed over a prolonged time period. For the NK92 cells in this study, we employ the second option. By comparing a region of the collagen matrix before and after an NK cell has passed through, we confirm that these cells do not permanently remodel the matrix (Supplementary Video 9).

For the OpenPIV algorithm, we used a window size of 12 µm with an overlap of 60% (corresponding to an element size of 4.8 µm). Deformation vectors with low confidence (defined by OpenPIV for a ratio <1.3 between the global maximum of the image cross-correlation divided by the second-highest local maximum value) were ignored. The accuracy with which we can measure matrix deformations with our set-up is estimated by imaging collagen gels without cells. We recorded image stacks at 28 non-overlapping positions in the gel (each 123 × 123 × 123 µm), each over a period of 23 min with a time interval of 1 min and a voxel size of 0.24 × 0.24 × 1 µm as in the cell experiments. We then computed the deformation field at every voxel position as described above, and the accuracy (noise level) was calculated as the standard deviation σ of all deformation values, separately evaluated in x, y and z directions. We obtained values of $\sigma_x = 41$ nm, $\sigma_y = 42$ nm ad $\sigma_z = 99$ nm. As an alternative to confocal reflection image stacks, matrix deformations can also be measured from image stacks of hydrogels with embedded microbeads (Fig. 4c and Supplementary Fig. 6), or from bright-field image stacks without beads but with sufficient image contrast to detect the diffraction pattern around collagen fibres (Extended Data Fig. 7 and Supplementary Video 13).

Cell tracking

The cell shape and position at each time point were extracted from intensity-projected bright-field image stacks. We computed the local entropy of the band-pass filtered images, subtracted the background using regional maxima filtering, binarized the image using Otsu thresholding[59] and applied binary morphological operations to remove small objects and holes. From the binarized object (which is the segmented cell), we calculated the area, the x,y position (centre of mass) and the aspect ratio, defined here as the major axis divided by the minor axis of an ellipse fitted to the cell shape. If a cell reached the edges of the image, this cell was not tracked further. The migration speed was calculated from the cell positions across subsequent images. The migration distance was calculated as the diagonal of the smallest rectangle containing the cell trajectory. Only trajectories containing at least 20 data points (19 min) were included in the analysis.

Correlation analysis

We cross-correlated the time development of cellular contractility, cell speed, cell minor axis normalized to the cell size (square root of the cell area), and cell aspect ratio for all NK92 cells under control conditions (Fig. 2d). As cell velocity and cell forces are calculated from the difference in cell position and matrix deformations between two consecutive image stacks, whereas the minor axis and aspect ratio are obtained for each single image stack, we linearly interpolated the minor axis and aspect ratio between two consecutive image stacks before cross-correlation. We then calculated the Spearman rank correlation coefficient between speed and contractility, between speed and aspect ratio, and between contractility and aspect ratio, for time shifts from −7 min to +7 min. The error intervals were determined using bootstrapping with a sample size of 1,000. For computing cross-correlations of speed and aspect ratio with the contractility signal, only time points with positive contractility were considered.

Force reconstruction

To solve the inverse problem of reconstructing cellular forces $\mathbf{f}$ from the measured 3D deformation field $\mathbf{U}^{\mathrm{meas}}$ (equation (5)), we used an iterative approach that varies the simulated matrix deformation field $\mathbf{U}$ with the aim to minimize a target function $L(\mathbf{U})$. This target function was computed from the difference between the simulated matrix deformations $\mathbf{U}$ and the measured matrix deformations, $\mathbf{U}^{\mathrm{meas}}$, plus a Thikonov regularization term $|\mathbf{f}(\mathbf{U})|^2$ (refs. 12,60,61) to constrain the force field $\mathbf{f}$:

$$L(\mathbf{U}) = |\mathbf{U} - \mathbf{U}^{\mathrm{meas}}|^2 + A \cdot |\mathbf{f}(\mathbf{U})|^2 \tag{6}$$

The force field $\mathbf{f}$ is computed from the simulated deformation field $\mathbf{U}$ using equation (5). The diagonal regularization factor matrix A has weights that favour large forces (presumably generated by the cell) and penalizes small forces (presumably caused by measurement noise)[12,62] (equation (7)). At the boundary (surface of the simulated volume), we set the regularization factor to zero (see 'Boundary forces' section). The index i represents the nodes of the finite-element mesh.

$$A_{ii} = \begin{cases} \alpha, & \text{if } |\mathbf{f}_i| < 1.345 \cdot \mathrm{median}(|\mathbf{f}|) \\ \alpha \frac{1.345 \cdot \mathrm{median}(|\mathbf{f}|)}{|\mathbf{f}_i|}, & \text{if } |\mathbf{f}_i| \geq 1.345 \cdot \mathrm{median}(|\mathbf{f}|) \\ 0, & \text{if } i \in \text{Boundary} \end{cases} \tag{7}$$

As $f(\mathbf{U})$ is nonlinear, $L(\mathbf{U})$ cannot be minimized easily. We apply a first-order Taylor series expansion of the displacement $\mathbf{U}$ ($\mathbf{U} + \Delta\mathbf{U}$), using the stiffness matrix K (equation (4))[52,61].

$$L(\mathbf{U}) = \left(|\mathbf{U} + \Delta\mathbf{U} - \mathbf{U}^{\mathrm{meas}}|^2 + A \cdot |(\mathbf{f}(\mathbf{U}) + K(\mathbf{U}) \cdot \Delta\mathbf{U})|^2 \right) \tag{8}$$

The $\Delta\mathbf{U}$ that minimizes this equation satisfies the following normal equation[61].

$$\underbrace{(\mathbf{I} + K(\mathbf{U}) \cdot A \cdot K(\mathbf{U}))}_{A_{ij}} \cdot \underbrace{\Delta\mathbf{u}}_{x_j} = \underbrace{\mathbf{U}^{\mathrm{meas}} + K(\mathbf{U}) \cdot A \cdot \mathbf{f}(\mathbf{U})}_{b_i} \quad (9)$$

This linear equation (of the form $A_{ij}x_j = b_i$) is solved using the conjugate gradient method to obtain a value for $\Delta\mathbf{U}$. Because of the pronounced nonlinearity of the problem, for the next iteration cycle we update the simulated deformation field only by a fraction (stepper) of $\Delta\mathbf{U}$ (typically 0.33):

$$\mathbf{U}' = \mathbf{U} + \mathrm{stepper} \cdot \Delta\mathbf{U}. \quad (10)$$

With the new displacement $\mathbf{U}'$, the stiffness matrix $K(\mathbf{U}')$ (equation (4)), the nodal forces $\mathbf{f}(\mathbf{U}')$ (equation (5)) and the weight matrix $A(\mathbf{f}(\mathbf{U}'))$ (equation (7)) are updated, and the linear Taylor expansion (equation (9)) is solved again. This procedure is iterated until the total energy $E(\mathbf{U})$ (equation (3)) of the system converges. Convergence is reached when the standard deviation of $E(\mathbf{U})$ divided by the mean of $E(\mathbf{U})$ (coefficient of variation) for the last 6 iterations is below a convergence criterion τ (typically 0.01).

From the resulting force vectors $\mathbf{f}_i$ at all nodes i, we compute the coordinates of the force epicentre $\mathbf{c}$. To find it, we minimize the magnitude Q of the cross product of the force field $\mathbf{f}_i$ with the vectors from the nodes $\mathbf{r}_i$ pointing to the epicentre coordinates $\mathbf{c}$ (refs.12,52):

$$Q = \sum_i |\mathbf{f}_i \times (\mathbf{r}_i - \mathbf{c})| \quad (11)$$

We determine the cellular contractility as the sum of the projected forces in the direction of the force epicentre[12,52]:

$$\mathrm{Contractility} = \sum_i \frac{\langle \mathbf{f}_i \cdot (\mathbf{r}_i - \mathbf{c}) \rangle}{|\mathbf{r}_i - \mathbf{c}|} \quad (12)$$

In this study, we performed the force reconstruction of migrating NK92 cells using the regularization parameter $\alpha = 10^{10}$ (equation (7)), which maximizes contractility and is stable against noise both for the experimental set-up and for simulated cells (Supplementary Fig. 13). We interpolated the 3D matrix deformations onto a cubic grid with a grid size of 4 µm (in the case of single cells, or larger as specified), and tessellate cubes into 6 tetrahedra (Supplementary Fig. 14). Time steps with unusually large z deformations, where the z components of the deformation vectors exceed 45% of the total deformations on average, were discarded. Such large z deformations can result from an occasional desyncronization between galvo stage movements and the movements of the confocal scanner.

For drug screening, we used 10 µM Rho-kinase inhibitor Y-27632 (Sigma-Aldrich), 3 µM non-muscle myosin II inhibitor blebbistatin (Sigma-Aldrich), 3 µM FAK inhibitor Defactinib (Cayman Chemicals) and 10 µg ml^{-1} anti-integrin blocking β1 antibody P5D2 (Abcam). Drugs remained in the culture medium during the measurements. For control cells, an equivalent amount of solvent (PBS or DMSO) or isotpye control antibodies (mouse IgG1 isotype control, R&D Systems) was added to the culture medium. Drug-treated and control samples are measured intermittently throughout a measurement day. Each experiment was repeated on three different days.

Boundary forces

Because the boundary of the simulated, finite-sized volume was fixed, the reconstructed force field contains cell-generated forces from the bulk, as well as distributed counter-forces from the surrounding matrix that appear at the volume boundary. The individual force vectors of the counter-forces are small compared with cell forces. Hence, the small-force penalization scheme (equation (7), first and second case) would bundle them into fewer, larger force vectors located in the bulk where they could interfere with cell forces. To avoid this, we set the regularization weights A_{ii} to zero for all tetrahedral mesh nodes at the boundary (surface) of the simulated volume (equation (7), third case). Hence, we excluded the surface of the mesh from the regularization cost function so that virtually all counter-forces appear only at the volume boundary and not in the bulk (Fig. 1a). Saenopy can therefore directly sum all the forces in the bulk of the mesh as they are contractile cell forces, without the need to arbitrarily define a maximum radius around the cell centre for the summation of forces. This improves robustness and accuracy especially for small stack sizes (Fig. 1c,e).

Simulations of force-generating dipoles and quadrupoles

We simulated the 3D deformation fields around force-generating dipoles and quadrupoles in a 1.2 mg ml^{-1} collagen matrix (batch A; Extended Data Fig. 2) with the iterative scheme described above, with the following modifications. The displacements at the mesh boundary were set to zero, the forces at the dipole or quadrupole points were given, and the forces in the bulk were set to zero. To simulate contractile dipoles, we added two opposing point forces ($\mathbf{f}^{\mathrm{ext}}$) with a distance of 15 µm or 30 µm. To simulate contractile quadrupoles, we added 4 inward-pointing forces ($\mathbf{f}^{\mathrm{ext}}$) at the nodes of a regular tetrahedron with an edge length of 15 µm or 30 µm. We then iteratively varied the deformation field until the simulated forces matched the imposed force field using the conjugate gradient method as described above. However, instead of equation (9), we solved the following equation:

$$\underbrace{K(\mathbf{U})}_{A} \cdot \underbrace{\Delta\mathbf{U}}_{x} = \underbrace{\mathbf{f}(\mathbf{U}) - \mathbf{f}^{\mathrm{ext}}}_{b} \quad (13)$$

and updated the deformation field $\mathbf{U}$ after each iteration according to equation (10), as well as the stiffness matrix $K(\mathbf{U})$ (equation (4)) and the nodal forces $\mathbf{f}(\mathbf{U})$ (equation (5)), until the total energy $E(\mathbf{U})$ converged[12,52].

Point forces were applied to the nearest possible nodes for a grid size of 4 µm and a stack volume of (150 µm)^3. We simulated various contractilities (2–400 nN) with or without added Gaussian noise with a defined standard deviation σ to the deformation field.

To benchmark the accuracy of different 3D TFM reconstruction methods (Fig. 5), we simulated the collagen deformations around artificial cells according to equation (13) and then performed force reconstruction. Axon growth cones were simulated by monopoles, immune cells, hepatic stellate cells and cancer cells by dipoles, and intestinal organoids by dodecahedrons, each with corresponding contractilities, spatial dimensions and material parameters taken from experiments. For force reconstruction, we used standard Saenopy (boundary method), Saenopy in combination with a purely linear elastic material model (linear method), and Saeno (maximum distance method, whereby r_{max} is optimized for the best possible agreement of simulated and reconstructed contractility values).

Magnetic tweezer experiments

Data from magnetic tweezer experiments were obtained from a previous study[12]. In brief, a magnetic tweezer was used to apply forces to microbeads (5 µm superparamagnetic beads, Microparticles) that were embedded in a collagen gel. We analysed a dataset of 14 microbeads with forces between 8 nN and 23 nN. Image stacks (433 × 433 × 100 µm) were taken before and after force application. From the image stacks, we determined the matrix deformations of 1-µm-sized fluorescent beads (FluoSpheres, Molecular Probes) using Saenopy with a PIV window size of 42 µm and a PIV element size of 14 µm. We then reconstructed contractile forces using linear Saenopy (boundary method, linear elastic material model without parameters λ_s, d_0 and d_s), nonlinear Saeno (maximum distance r_{max}) and nonlinear Saenopy (boundary method)

using the regularization parameter $\alpha = 10^{10}$, an element size of 14 µm and a reconstruction volume of 700 × 700 × 350 µm. The overall force was calculated by individually summing the x, y and z components of the reconstructed force vectors and then taking the absolute value of the resulting total force vector.

Limitations

Resolution/heterogeneities. The spatial resolution of the recovered cellular forces is limited by the pores size of the matrix, which in turn limits the window size of the PIV algorithm and the size of the finite elements. Moreover, the fibrous structure of the matrix naturally introduces local heterogeneities at length scales even above the pore size. Therefore, the spatial resolution is on the order of 5–10 times the average pore size, that is, around 30 µm in collagen gels[12]. However, deformations in collagen are propagated over long distances within the matrix so that the global contractility of the cell can still be accurately recovered.

Viscoelasticity/plasticity. The material model of our method accounts for nonlinear elastic matrix deformations, but ignores viscoelastic or plastic properties. This is justified for moderate strains (below 20%) where collagen behaves predominantly as an elastic material (Extended Data Fig. 3). Moreover, after drug-induced relaxation of cellular forces, the recoil of the matrix deformations are driven by the release of elastically stored strain energy so that an elastic material model is appropriate. Potential problems arise only if the force-free matrix configuration is calculated from images taken at the beginning of the experiment (or from the median deformations) so that non-elastic matrix deformations, if present, can contribute to the total deformations. In this case, a purely elastic model overestimates the forces. For highly motile immune cells, however, we do not observe permanent deformations of the collagen matrix after the cell has migrated through it.

Statistical analysis

For comparing two samples, we used a two-sided Student's t-test with $P < 0.05$ and $P < 0.01$ as specified in the figures. For statistical analysis involving multiple comparisons, we used a Kruskal–Wallis test[63] and confirm significance for $P < 0.05$. P values are adjusted using Bonferroni correction[51], as indicated in the figures. Error intervals and significance for correlations (Fig. 2d), as well as for testing drug effects on contractility and migration (Fig. 3a), were determined using bootstrapping with a sample size of 1,000 for the data in Fig. 2d, and 100,000 for the data in Fig. 3a. Statistical analysis was performed using the Python packages SciPy[64] and NumPy[65]. Note that the standard error of speed, distance or contractility across an individual cell is larger than the standard error across the mean values of independent experiments. In this case, performing statistics over individual cells better reflects the uncertainty of the measurements compared with performing statistics over independent experiments.

Reporting summary

Further information on research design is available in the Nature Portfolio Reporting Summary linked to this article.

Data availability

Source data from this study are are provided with this paper and as part of the Saenopy GitHub repository[50]. Image raw data are available upon request from the corresponding author.

Code availability

The software (Saenopy) and all dependent packages are available on GitHub as an open-source Python package with a graphical user interface[50]. Figures are created using the Python packages Pylustrator[66] and PyVista[67] using a colourblind-friendly colour palette from ref. 68.

References

52. Steinwachs, J. *Cellular Forces during Migration through Collagen Networks*. PhD thesis, Friedrich-Alexander-Universität Erlangen-Nürnberg (2015).
53. Kah, D. et al. A low-cost uniaxial cell stretcher for six parallel wells. *HardwareX* **9**, e00162 (2021).
54. Faust, U. et al. Cyclic stress at mHz frequencies aligns fibroblasts in direction of zero strain. *PLoS ONE* **6**, e28963 (2011).
55. Koser, D. E. et al. Mechanosensing is critical for axon growth in the developing brain. *Nat. Neurosci.* **19**, 1592–1598 (2016).
56. Nieuwkoop, P. D. & Faber, J. *Normal Table of* Xenopus laevis *(Daudin): A Systematical and Chronological Survey of the Development from the Fertilized Egg till the End of Metamorphosis* (Garland, 1994).
57. Mark, C. et al. Collective forces of tumor spheroids in three-dimensional biopolymer networks. *eLife* **9**, e51912 (2020).
58. Martínez-Sánchez, L. D. C. et al. Epithelial RAC1-dependent cytoskeleton dynamics controls cell mechanics, cell shedding and barrier integrity in intestinal inflammation. *Gut* **72**, 275–294 (2023).
59. Otsu, N. A threshold selection method from gray-level histograms. *IEEE Trans. Syst. Man Cybern.* **9**, 62–66 (1979).
60. Tikhonov, A. N., Goncharsky, A. V., Stepanov, V. V. & Yagola, A. G. *Numerical Methods for the Solution of Ill-Posed Problems* (Springer Science & Business Media, 1995).
61. Tikhonov, A. N. On the stability of inverse problems. *Proc. USSR Acad. Sci.* **39**, 195–198 (1943).
62. Huber, P. J. *Robust Statistics* Vol. 523 (John Wiley & Sons, 2004).
63. Kruskal, W. H. & Wallis, W. A. Use of ranks in one-criterion variance analysis. *J. Am. Stat. Assoc.* **47**, 583–621 (1952).
64. Virtanen, P. et al. SciPy 1.0: fundamental algorithms for scientific computing in Python. *Nat. Methods* **17**, 261–272 (2020).
65. Harris, C. R. et al. Array programming with NumPy. *Nature* **585**, 357–362 (2020).
66. Gerum, R. Pylustrator: code generation for reproducible figures for publication. *J. Open Source Softw.* **5**, 1989 (2020).
67. Sullivan, C. & Kaszynski, A. PyVista: 3D plotting and mesh analysis through a streamlined interface for the Visualization Toolkit (VTK). *J. Open Source Softw.* **4**, 1450 (2019).
68. Wong, B. Points of view: color blindness. *Nat. Methods* **8**, 441 (2011).
69. Kroy, K. & Frey, E. Force-extension relation and plateau modulus for wormlike chains. *Phys. Rev. Lett.* **77**, 306–309 (1996).
70. Jansen, K. A. et al. The role of network architecture in collagen mechanics. *Biophys. J.* **114**, 2665–2678 (2018).
71. Lang, N. R. et al. Estimating the 3D pore size distribution of biopolymer networks from directionally biased data. *Biophys. J.* **105**, 1967–1975 (2013).
72. Krauss, P., Metzner, C., Lange, J., Lang, N. & Fabry, B. Parameter-free binarization and skeletonization of fiber networks from confocal image stacks. *PLoS ONE* **7**, e36575 (2012).
73. Sato, Y. et al. Three-dimensional multi-scale line filter for segmentation and visualization of curvilinear structures in medical images. *Med. Image Anal.* **2**, 143–168 (1998).
74. Yen, J. C., Chang, F. J. & Chang, S. A new criterion for automatic multilevel thresholding. *IEEE Trans. Image Process.* **4**, 370–378 (1995).

Acknowledgements

This work was funded by the German Research Foundation (DFG; project 326998133 – TRR-SFB 225 – subprojects A01, B09 and C02; project 460333672 – CRC 1540 – subprojects A01, A05, B02 and C05; project 375876048 – TRR-SFB 241 – subprojects A07 and C04; project 461063481 – LO 2465/6-1; project 414058251 – SPP-1782, LO 2465/2-1), the National Institutes of Health (HL120839), the Emerging Fields

Initiative of the University of Erlangen-Nuremberg and the Alexander von Humboldt Foundation (Humboldt Professorship, K.F.). We thank the ENB Biological Physics programme of the University Bayreuth for support, R. Henriques for the LaTeX layout, I. Thievessen for help with differential interference contrast imaging and R. Reimann for designing the Saenopy logo.

Author contributions

Methodology: R.G., D.B., M.C., B.F. and C.M. Software: R.G., D.B., M.C. and A.B. Rheology: D.B., M.C., L.B., S.B. and N.G. Immune cell experiments: L.B., T.C., D.B. and C.V. Organoid experiments: P.A.N., D.B. and R.L.-P. Neuronal cell experiments: K.F. and N.G. Data analysis: D.B., L.B., C.M. and R.G. Writing: D.B., B.F., M.C., C.M. and R.G.

Competing interests

The authors declare no competing interests.

Additional information

Extended data is available for this paper at https://doi.org/10.1038/s41567-024-02632-8.

Supplementary information The online version contains supplementary material available at https://doi.org/10.1038/s41567-024-02632-8.

Correspondence and requests for materials should be addressed to Ben Fabry.

Peer review information *Nature Physics* thanks Hawa Racine Thiam, Karin Wang and the other, anonymous, reviewer(s) for their contribution to the peer review of this work.

https://doi.org/10.1038/s41567-024-02632-8

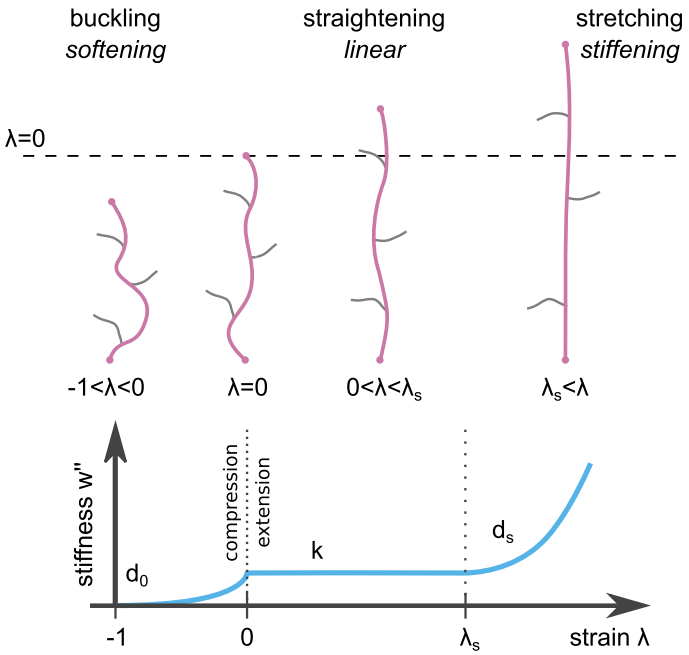

Extended Data Fig. 1 | Nonlinear material model. The nonlinear material model divides the mechanical response of individual fibers into a region where fiber stiffness ($\omega^{\sim}$) decreases exponentially with decreasing strain under compression (buckling), a region of constant fiber stiffness for small strains (straightening), and a region of exponentially increasing fiber stiffness for larger strains (stretching)[12]. Non-linear materials are modelled according to Eq. (1) using four material parameters: The linear stiffness k_0, the buckling coefficient d_0, the characteristic strain λs, and the stiffening coefficient ds. For small extensional strain in the linear range ($0 < \lambda < \lambda s$), fibers exhibit a constant stiffness k. For compressive strain ($-1 < \lambda < 0$), fibers buckle and show an exponential decay of the stiffness with a characteristic buckling coefficient d_0. For larger extensional strain beyond the linear range ($\lambda s < \lambda$), the fibers show strain stiffening with an exponential increase of stiffness with a characteristic stiffening coefficient ds. Dashed lines indicate the different regimes. Figure adapted with permission from ref. 12, Springer America Inc.

https://doi.org/10.1038/s41567-024-02632-8

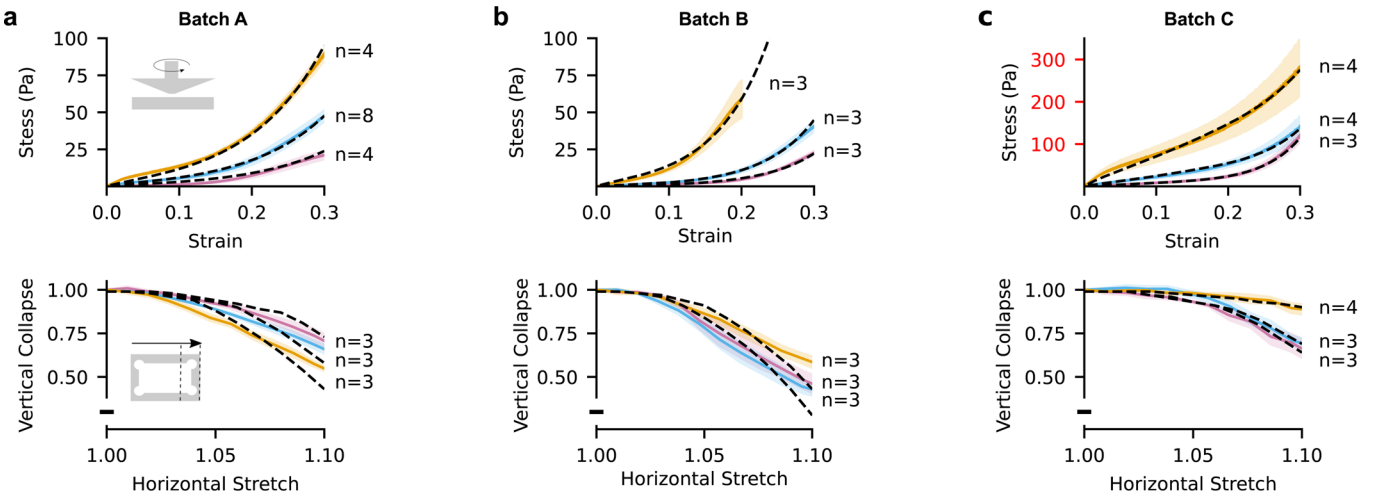

d

	k_0	λ_s	d_s	d_0
Collagen 0.6mg/ml (Batch A)	725	0.0320	0.055	0.0030
Collagen 1.2mg/ml (Batch A)	1449	0.0320	0.055	0.0022
Collagen 2.4mg/ml (Batch A)	2899	0.0320	0.055	0.0015
Collagen 0.6mg/ml (Batch B)	293	0.0230	0.036	0.0013
Collagen 1.2mg/ml (Batch B)	590	0.0230	0.036	0.0013
Collagen 2.4mg/ml (Batch B)	3162	0.0230	0.036	0.0018
Collagen 0.6mg/ml (Batch C)	2045	0.0542	0.027	0.0023
Collagen 1.2mg/ml (Batch C)	6062	0.0804	0.034	0.0025
Collagen 2.4mg/ml (Batch C)	16034	0.0951	0.050	0.0070
Collagen 0.6mg/ml (Steinwachs et al.)	447	0.0075	0.033	0.0008
Collagen 1.2mg/ml (Steinwachs et al.)	1645	0.0075	0.033	0.0008
Collagen 2.4mg/ml (Steinwachs et al.)	5208	0.0075	0.033	0.0008

Collagen 0.6 mg/ml
Collagen 1.2 mg/ml
Collagen 2.4 mg/ml
model

Extended Data Fig. 2 | Rheology and material model for collagen Batch A, B, C. Collagen hydrogels from three different batches (**a**, **b**, **c**) at different concentrations of 0.6 mg/ml (purple), 1.2 mg/ml (blue), and 2.4 mg/ml (orange) are characterized using cone-plate shear-rheological measurements (top; inset shows schematic of experimental setup) and uniaxial stretch-experiments (bottom; inset shows schematic of experimental setup) as described in the Methods section of the main text. The solid lines represent the mean value and the shaded areas represent the standard error for N individual samples. Dashed lines show the fit of the finite element model to the averaged data per condition. The red axis label in **c** indicates different scaling compared to **a**, **b**. **d**, Material model parameters (Extended Data Fig. 1) for non-linear elastic biopolymers (linear stiffness k_0, the buckling coefficient d_0, the characteristic strain λs, and the stiffening coefficient ds.) for each condition. Previously measured parameters from Steinwachs et al.[12] are given for comparison. For each batch, we performed both individual fits to the data for each concentration separately, or global fits where the parameters λs, ds, and d_0 were the same for all or some of the concentrations. Global fit parameters were preferred if the fit quality was comparable to individual fits, in order to reduce the number of free fit parameters. The increased stiffness of collagen batch C compared to batch A and B is consistent with the observation of decreased cell-generated deformations (Extended Data Fig. 5). These stiffness differences can be attributed to batch-to-batch variation. Model parameters for 1.2 mg/ml collagen gels of Batch A were previously published in ref. 58.

https://doi.org/10.1038/s41567-024-02632-8

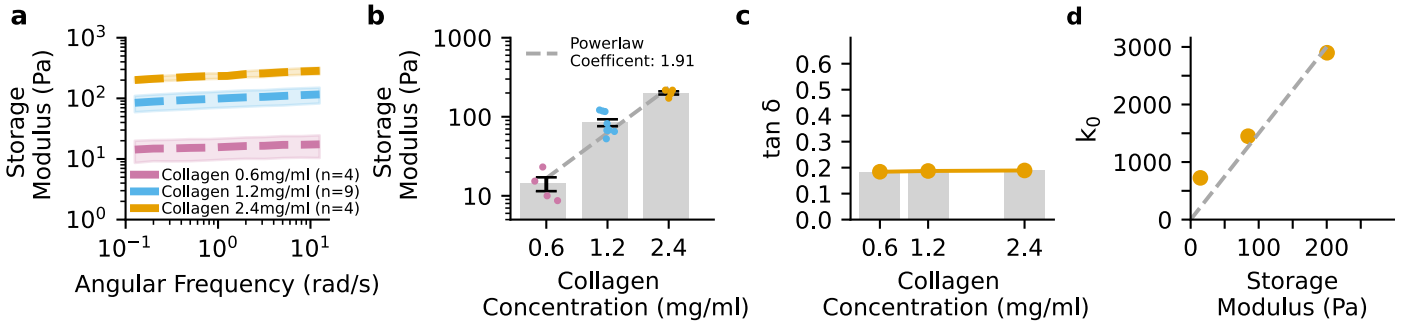

Extended Data Fig. 3 | Small amplitude rheology. a, Storage modulus derived from frequency sweeps with a cone-plate shear-rheometer at 1% strain amplitude for different collagen concentrations (Batch A, see Extended Data Fig. 2). Dashed lines indicate mean values, and shaded area indicate } one standard deviation. N indicates the number of collagen gels, where each gel was measured in an independent experiment. **b**, Storage modulus (mean value at 0.02 Hz) scales with collagen concentration according to a power-law with exponent of 1.91 in agreement to previously predicted and measured values[69,70]. Bars indicate mean } se and dashed line indicates powerlaw fit curve. Individual collagen gels are shown as dots. The sample size is the same as in a. **c**, Loss tangent δ (loss modulus G'' divided by storage modulus G', averaged between 0.02-2 Hz from the data presented in a) remains below 0.2 for all collagen concentrations,indicating predominantly elastic behavior. **d**, The FE model parameter k_0 (indicating the linear stiffness of the collagen fibers) for different collagen concentrations (see Extended Data Fig. 2) increases approximately linearly with the storage modulus G' of the collagen gels (measured at 0.02 Hz at a strain amplitude of 1% as shown in a). The gray dashed line indicates the predication from continuum mechanics, where $k_0 = 6E$, with Young's modulus $E = 2G(1+\nu)$ and Poisson ratio $\nu = 0.25$ for linear elastic, isotropic fiber networks[12]. Hence, $k_0 = 15G$.

https://doi.org/10.1038/s41567-024-02632-8

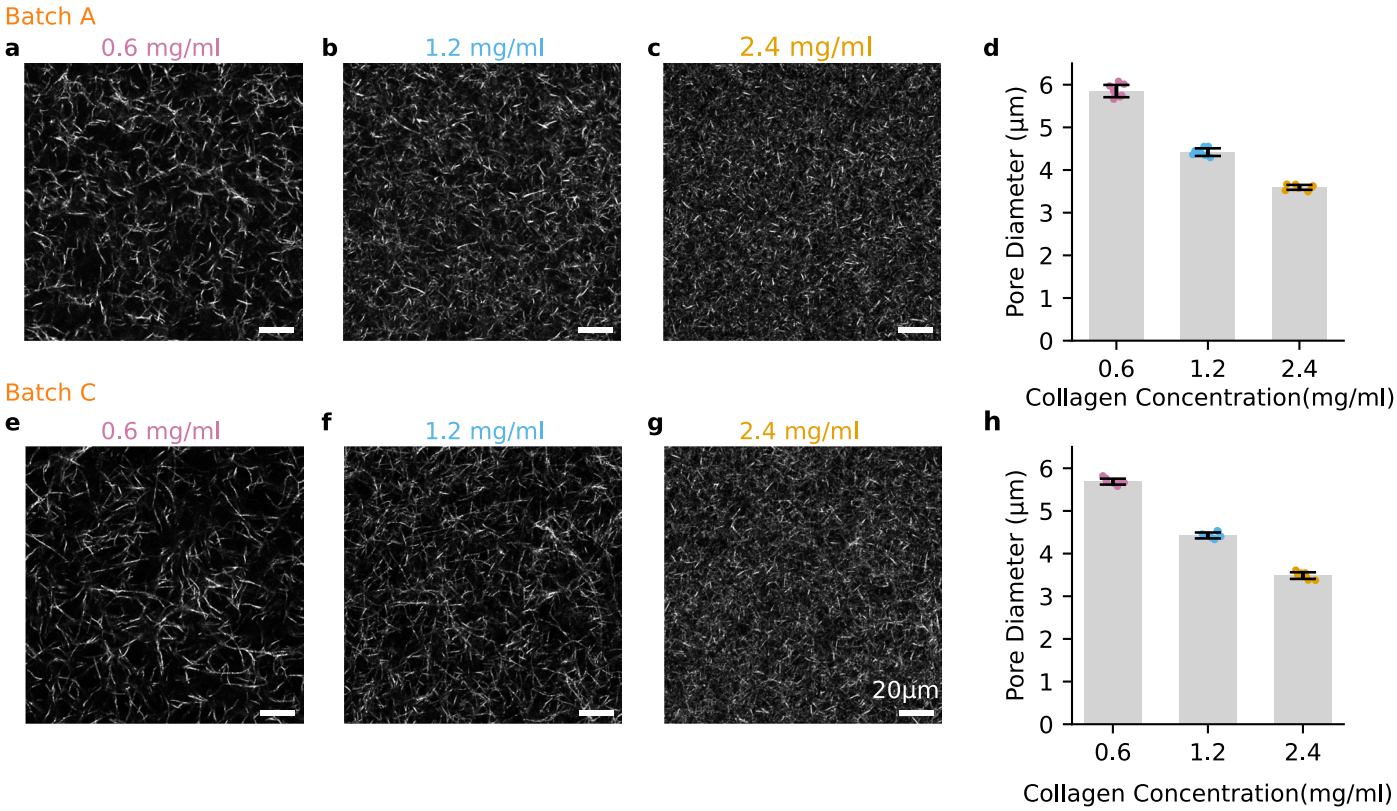

	0.6mg/ml	1.2mg/ml	2.4mg/ml
Batch A (Pore Diameter in μm)	5.85±0.14	4.42±0.09	3.59±0.06
Batch C (Pore Diameter in μm)	5.69±0.07	4.43±0.07	3.49±0.08

Extended Data Fig. 4 | Microstructure of collagen networks. The collagen fiber structure of two different collagen batches (**a**-**c**: Batch A; **e**-**g**: Batch C) is imaged using confocal reflection microscopy for three different collagen concentrations (imaged volume of 160x160x200 μm with voxel-sizes of 0.314x0.314x0.642 μm). Grayscale images show a single slice of the imaged volume.3D pore diameters are computed from the covering radius transform as described in[71,72]. The mean pore diameters for each collagen concentration (**d**, **h**) are calculated from 8 different regions within an stack (80x80x100 μm with 0.314x0.314x0.642 μm voxel-size). The error bars represent the standard deviation of the mean pore diameter between different regions (shown as individual points) of the imaged stack. Mean value and standard deviation of the pore diameters are listed in the table. See SI Video 1 for 3D representations of the collagen fiber networks.

https://doi.org/10.1038/s41567-024-02632-8

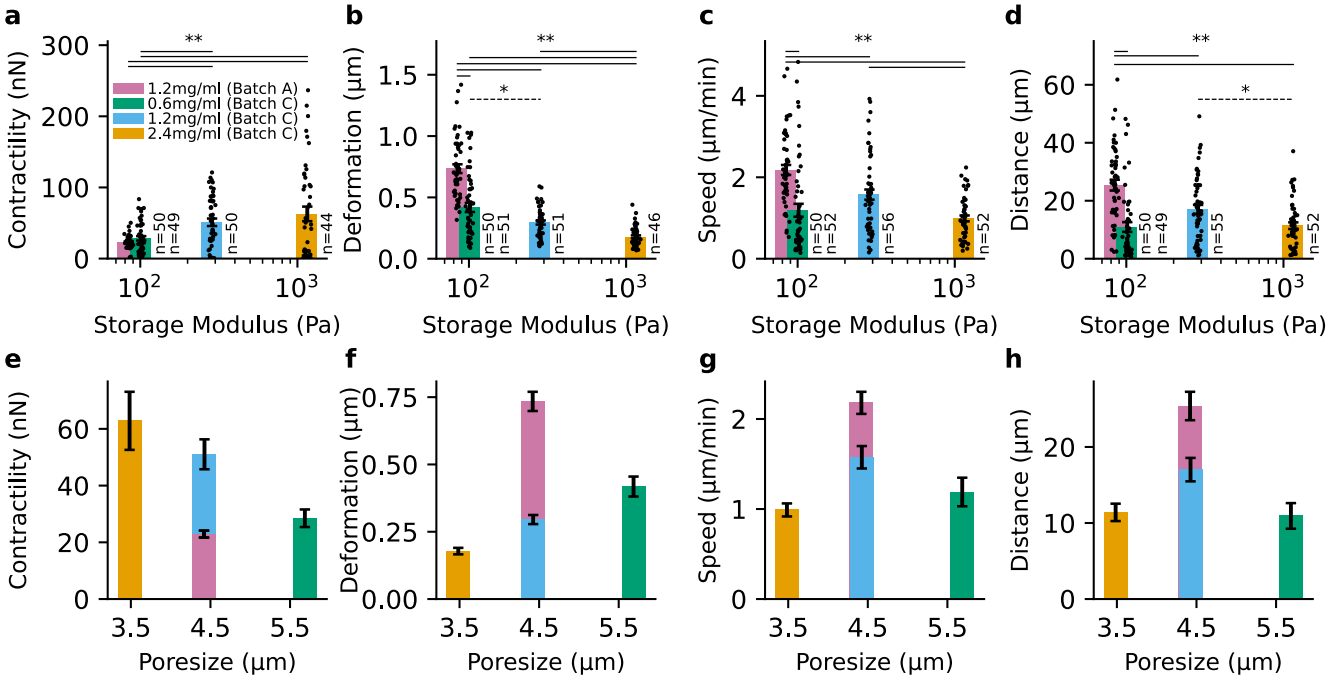

Extended Data Fig. 5 | Dependence of immune cell migration and force generation on matrix stiffness and pore size. Cell contractility (**a**, **e**), matrix deformations (**b**, **f**), cell speed (**c**, **g**), and cell travelled distance (**d**, **h**) are measured in collagen gels (0.6 mg/ml, 1.2 mg/ml, and 2.4 mg/ml from different collagen batches) with different stiffnesses (**a**-**d**) and pore sizes (**e**-**h**). The storage modulus of different collagen gels is measured with a cone-plate shear-rheometer at 0.02 Hz (1% strain amplitude, see Extended Data Fig. 3), and the pore size is derived from confocal reflection images(see Extended Data Fig. 4). Colored bars and error bars indicate mean }se for n individual cells (black points) from three (pink and orange bars) or four (green and blue bars) independent experiments. * indicates $p<0.05$ and ** indicates $p<0.01$ for two-sided t-test with Bonferroni correction[51]. For clarity, the legend, data points, statistical tests, and cell numbers are only shown in the top row. (**a**, **e**), Maximum contractility of each cell during a 23 min measurement period. (**b**, **f**), Maximum of the absolute matrix deformation vector (99% percentile) of each cell during a 23 min measurement period. (**c**, **g**), Mean cell speed during a 23 min measurement period. (**d**, **h**), Migration distance of cells after 23 min in 1.2 mg/ml collagen gels. Distance is calculated as the diagonal of the smallest rectangle containing the cell trajectory. Here, only trajectories containing at least 20 data points (corresponding to trajectories of at least 19 min duration) are included in the analysis. Cell contractility monotonically increases, and matrix deformation monotonically decreases with matrix stiffness. Migration speed and travelled distance show a maximum response at intermediate pore sizes.

https://doi.org/10.1038/s41567-024-02632-8

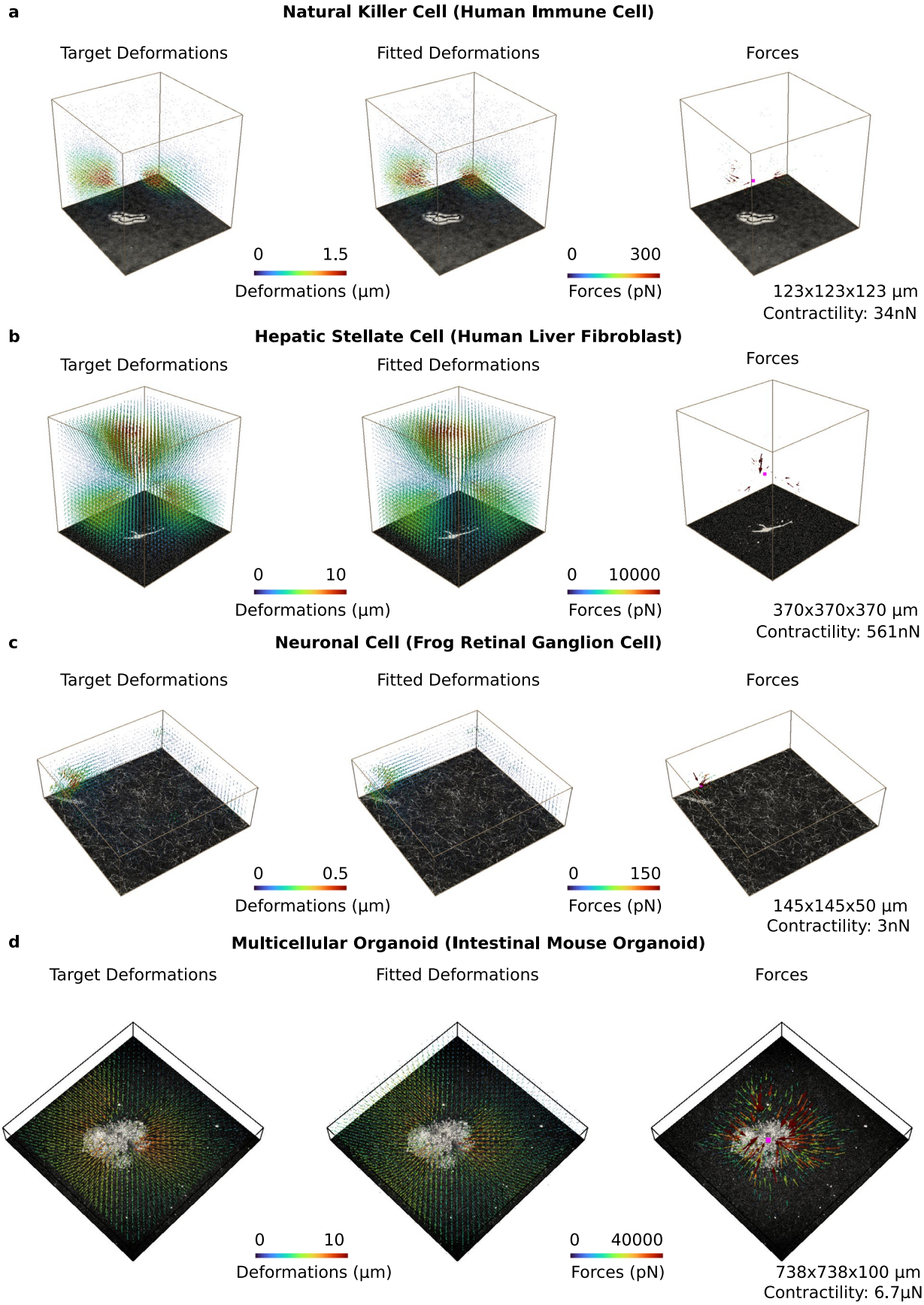

Extended Data Fig. 6 | See next page for caption.

https://doi.org/10.1038/s41567-024-02632-8

Extended Data Fig. 6 | Force reconstitution for different cell types. For different cell types, cell-generated matrix deformations are measured and then interpolated onto a finite-element mesh (left). The reconstructed matrix deformations (center) and forces (right) are obtained using Saenopy. The force epicenter is shown in pink, and the size of the image stack is indicated in the lower right. **a**, Human natural killer cell (NK92) embedded in a 1.2 mg/ml collagen gel (Batch A) during a contractile phase (Fig. 2, SI Videos 6–8). **b**, Hepatic stellate cell (human liver fibroblast) in a 1.2 mg/ml collagen gel (Batch C) after 2 days of culture (SI Video 11). **c**, Axon growth cones of a frog retinal ganglion cell embedded in a 1.0 mg/ml collagen gel (Batch D) during a contractile phase (SI Video 10). **d**, Mouse intestinal organoid in a 1.2mg/ml collagen gel (Batch C) after 24 hours. Time-lapse images of organoid contraction and drug-induced relaxation are shown in SI Video 12.

https://doi.org/10.1038/s41567-024-02632-8

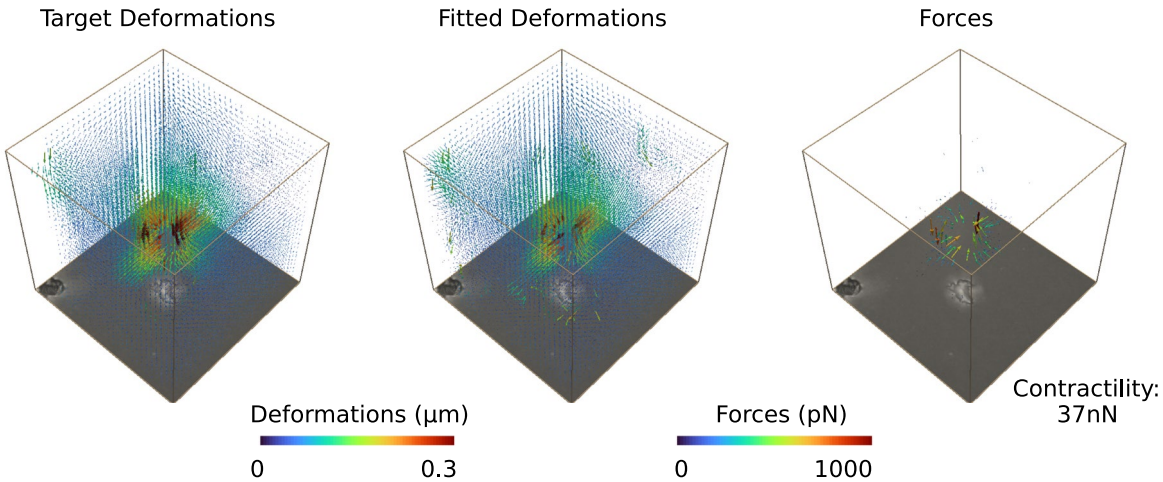

Extended Data Fig. 7 | Saenopy resolves 3D force fields from bright-field image stacks. Matrix deformations and forces around a NK92 cell embedded in a 1.2 mg/ml collagen gel (Batch C). Bright-field images are acquired with an ASI RAMM microscope (Applied Scientific Instrumentation, Eugene), CMOS-camera (acA4096-30um, Basler, Ahrensburg),and 20x objective (0.7NA, air, Olympus, Tokyo). The cells are kept at 37°C and 5% CO2 in a stage incubator (Tokai HIT, Fujinomiya). Matrix deformations (left) are calculated from bright-field image stacks (120 × 120 × 120 μm, with a voxel-size of 0.15 × 0.15 × 2 μm, dt = 30 s) during a contractile phase (SI Video 13, at t = 2 min). Cell forces (right) and corresponding matrix deformations (middle) are reconstructed using a regularization parameter of 10^{11}. Maximum intensity projected image stacks are shown below the 3D cubes.

nature portfolio

Corresponding author(s): Ben Fabry

Last updated by author(s): Jun 6, 2024

Reporting Summary

Nature Portfolio wishes to improve the reproducibility of the work that we publish. This form provides structure for consistency and transparency in reporting. For further information on Nature Portfolio policies, see our Editorial Policies and the Editorial Policy Checklist.

Statistics

For all statistical analyses, confirm that the following items are present in the figure legend, table legend, main text, or Methods section.

n/a	Confirmed	
☐	☒	The exact sample size (*n*) for each experimental group/condition, given as a discrete number and unit of measurement
☐	☒	A statement on whether measurements were taken from distinct samples or whether the same sample was measured repeatedly
☐	☒	The statistical test(s) used AND whether they are one- or two-sided *Only common tests should be described solely by name; describe more complex techniques in the Methods section.*
☒	☐	A description of all covariates tested
☒	☐	A description of any assumptions or corrections, such as tests of normality and adjustment for multiple comparisons
☐	☒	A full description of the statistical parameters including central tendency (e.g. means) or other basic estimates (e.g. regression coefficient) AND variation (e.g. standard deviation) or associated estimates of uncertainty (e.g. confidence intervals)
☐	☒	For null hypothesis testing, the test statistic (e.g. *F*, *t*, *r*) with confidence intervals, effect sizes, degrees of freedom and *P* value noted *Give P values as exact values whenever suitable.*
☒	☐	For Bayesian analysis, information on the choice of priors and Markov chain Monte Carlo settings
☒	☐	For hierarchical and complex designs, identification of the appropriate level for tests and full reporting of outcomes
☐	☒	Estimates of effect sizes (e.g. Cohen's *d*, Pearson's *r*), indicating how they were calculated

Our web collection on statistics for biologists contains articles on many of the points above.

Software and code

Policy information about availability of computer code

Data collection

-Leica SP5 confocal microscope with Leica LAS AF software.
-TA Instruments Discovery HR-2 Rheometer with Trios software

Data analysis

-Scipy (Version 1.10.1)
https://github.com/scipy/scipy

-Numpy (Version 1.23.5)
https://github.com/numpy/numpy

-TFM Lab (Version "TFMLAB_public" on Gitlab)
https://gitlab.kuleuven.be/MAtrix/Jorge/tfmlab_public

-OpenPIV Python (Version 0.22.2)
https://github.com/OpenPIV/openpiv-python

-Pylustrator (Version 1.2.1)
https://github.com/rgerum/pylustrator

-Pyvista (Version 0.37.0)
https://github.com/pyvista/pyvista

Our developed traction force method "Saenopy" is available as an open-source python package (https://github.com/rgerum/saenopy)

For manuscripts utilizing custom algorithms or software that are central to the research but not yet described in published literature, software must be made available to editors and reviewers. We strongly encourage code deposition in a community repository (e.g. GitHub). See the Nature Portfolio guidelines for submitting code & software for further information.

Data

Policy information about availability of data

All manuscripts must include a data availability statement. This statement should provide the following information, where applicable:

- Accession codes, unique identifiers, or web links for publicly available datasets
- A description of any restrictions on data availability
- For clinical datasets or third party data, please ensure that the statement adheres to our policy

Data from this study are available as Supplementary Data and as part of the Saenopy Github repository (https://github.com/rgerum/saenopy). Image raw data are available upon request from the corresponding author.

Research involving human participants, their data, or biological material

Policy information about studies with human participants or human data. See also policy information about sex, gender (identity/presentation), and sexual orientation and race, ethnicity and racism.

Reporting on sex and gender	Not applicalbe
Reporting on race, ethnicity, or other socially relevant groupings	Not applicable
Population characteristics	Not applicable
Recruitment	Not applicable
Ethics oversight	Not applicable

Note that full information on the approval of the study protocol must also be provided in the manuscript.

Field-specific reporting

Please select the one below that is the best fit for your research. If you are not sure, read the appropriate sections before making your selection.

☒ Life sciences ☐ Behavioural & social sciences ☐ Ecological, evolutionary & environmental sciences

For a reference copy of the document with all sections, see nature.com/documents/nr-reporting-summary-flat.pdf

Life sciences study design

All studies must disclose on these points even when the disclosure is negative.

Sample size	The sample size was the maximum number of cells that could be imaged per day (typically 15 cells per condition) on three different days and cell passages, resulting in a total of approximately 50 cells per condition.
Data exclusions	For the correlation analysis of forces, we discarded time-points where the cells show negative contractility, as explained in Methods.
Replication	Experiments were repeated on 3 different days. Repetitions were successful and no repetition was excluded.
Randomization	All conditions were measured in an interleaved fashion throughout the day (e.g., 4 control cells for 23 min, then 4 ROCK inhibitor-treated cells, then 4 blebbistatin-treated cells, then back to 4 different control cells, etc.), so no additional randomization was necessary. Maintaining identical time intervals was considered more important.
Blinding	The investigators were not blinded to group allocation, as the same persons performed the measurement preparation and imaging. However, cell positions were stored prior to measurement (without prior knowledge of cell behavior) and then tracked over the measurement interval without excluding cells.

Reporting for specific materials, systems and methods

We require information from authors about some types of materials, experimental systems and methods used in many studies. Here, indicate whether each material, system or method listed is relevant to your study. If you are not sure if a list item applies to your research, read the appropriate section before selecting a response.

Materials & experimental systems

n/a	Involved in the study
☐	☒ Antibodies
☐	☒ Eukaryotic cell lines
☒	☐ Palaeontology and archaeology
☐	☒ Animals and other organisms
☒	☐ Clinical data
☒	☐ Dual use research of concern
☒	☐ Plants

Methods

n/a	Involved in the study
☒	☐ ChIP-seq
☒	☐ Flow cytometry
☒	☐ MRI-based neuroimaging

Antibodies

Antibodies used: Anti-integrin blocking β1 antibody P5D2 (cat. no. ab24693, Lot: GR3241225-7, Abcam, Cambridge). Mouse IgG 1 Isotype antibody (cat. no. MAB002, Lot: IX2921122, R&D Systems, Minneapolis) was used as control.

Validation: The antibody has been validated by the manufacturer (KO validation) and is commonly used in various studies.

Notes from manufacturer's website:
This monoclonal antibody to integrin beta 1 has been knockout validated in ICC/IF and flow cytometry. The expected signal was observed in wild type cells and no signal was seen in knockout cells. This antibody inhibits the function of beta 1 integrins and can be used to block cell adhesion (Dittell et al., 1993 and Yokosaki et al., 1994).

Further studies:
Inhibiting migration in human mesenchymal cancer cells
https://www.nature.com/articles/s41467-018-06641-z

Inhibiting adhesion of human B-cell precursors (to stromal cells)
https://doi.org/10.1182/blood.V81.9.2272.2272

Inhibiting adhesion of axon growth cones
10.1016/j.celrep.2020.107907

Eukaryotic cell lines

Policy information about cell lines and Sex and Gender in Research

Cell line source(s):
- NK92 cells (ATCC CRL-2407, Manassas, USA)
- Human hepatic stellate cells (HUCLS, Lonza, Basel)
- Primary intestinal organoids from C57BL/6J mouse (Strain #:000664, The Jackson Laboratory)
- Primary eye primordia explants are dissected from Xenopus laevis embryos

Authentication: No further authentication was performed.

Mycoplasma contamination: Possible mycoplasma contamination was tested at regular intervals with negative results.

Commonly misidentified lines (See ICLAC register): No commonly misidentified cell lines were used in the study.

Animals and other research organisms

Policy information about studies involving animals; ARRIVE guidelines recommended for reporting animal research, and Sex and Gender in Research

Laboratory animals:
- Primary intestinal organoids from C57BL/6J mouse (Strain #:000664, The Jackson Laboratory)
- Primary eye primordia explants are dissected from Xenopus laevis embryos

Wild animals: The study did not involve wild animals.

Reporting on sex	Sex was not a factor in the study design as we did not consider it to be relevant for the traction force method.
Field-collected samples	The study did not involve samples collected from the field.
Ethics oversight	Experiments involving mice have been approved by the Institutional Animal Care and Use Committee of the University of Erlangen-Nuremberg and by the Government of Mittelfranken (Würzburg, Germany). Xenopus experiments were conducted in accordance with the UK Animals (Scientific Procedures) Act 1986.

Note that full information on the approval of the study protocol must also be provided in the manuscript.